

Supernovae in the Subaru Deep Field: the rate and delay-time distribution of type Ia supernovae out to redshift 2

O. Graur,^{1*} D. Poznanski,^{2,3,4} D. Maoz,¹ N. Yasuda,⁵ T. Totani,⁶ M. Fukugita,⁵
A. V. Filippenko,³ R. J. Foley,^{3,7} J. M. Silverman,³ A. Gal-Yam,⁸ A. Horesh,⁹
and B. T. Jannuzi¹⁰

¹*School of Physics and Astronomy, Tel-Aviv University, Tel-Aviv 69978, Israel*

²*Lawrence Berkeley National Laboratory, 1 Cyclotron Rd., Berkeley, CA 94720, USA*

³*Department of Astronomy, University of California, Berkeley, CA 94720-3411, USA*

⁴*Einstein Fellow*

⁵*Institute for Cosmic Ray Research, University of Tokyo, Kashiwa 277-8582, Japan*

⁶*Department of Astronomy, School of Science, Kyoto University, Sakyo-ku, Kyoto 606-8502, Japan*

⁷*Harvard-Smithsonian Center for Astrophysics, 60 Garden St., Cambridge, MA 02138, USA*

⁸*Department of Particle Physics and Astrophysics, Weizmann Institute of Science, 76100 Rehovot, Israel*

⁹*Cahill Center for Astrophysics, California Institute of Technology, Pasadena, CA 91125, USA*

¹⁰*National Optical Astronomy Observatory, Tucson, AZ 85726-6732, USA*

30 January 2011

ABSTRACT

The type Ia supernova (SN Ia) rate, when compared to the cosmic star formation history (SFH), can be used to derive the delay-time distribution (DTD) of SNe Ia, which can distinguish among progenitor models. We present the results of a SN survey in the Subaru Deep Field (SDF). Over a period of 3 years, we have observed the SDF on four independent epochs with Suprime-Cam on the Subaru 8.2-m telescope, with 2 nights of exposure per epoch, in the R , i' , and z' bands. We have discovered 150 SNe out to redshift $z \approx 2$. Using 11 photometric bands from the observer-frame far-ultraviolet to the near-infrared, we derive photometric redshifts for the SN host galaxies (for 24 we also have spectroscopic redshifts). This information is combined with the SN photometry to determine the type and redshift distribution of the SN sample. Our final sample includes 26 SNe Ia in the range $1.0 < z < 1.5$ and 10 in the range $1.5 < z < 2.0$. As our survey is mostly insensitive to core-collapse SNe (CC SNe) at $z > 1$, most of the events found in this range are likely SNe Ia. Our SN Ia rate measurements are consistent with those derived from the *Hubble Space Telescope* (*HST*) GOODS sample, but they have statistical uncertainties that are 2–3 times smaller, of 30–50 per cent. Based on this sample, we find that the SN Ia rate evolution levels off at $1.0 < z < 2.0$, but shows no sign of declining. Combining our SN Ia rate measurements and those from the literature, and comparing to a wide range of possible SFHs, the best-fitting DTD (with a reduced $\chi^2 = 0.82$) is a power law of the form $\Psi(t) \propto t^\beta$, with index $\beta = -0.97^{+0.25}_{-0.28}$ (statistical) $^{+0.17}_{-0.18}$ (systematic). This result is consistent with other recent DTD measurements at various redshifts and environments, and is in agreement with a generic prediction of the double-degenerate progenitor scenario for SNe Ia. The number of SNe Ia per formed stellar mass, integrated over a Hubble time, is in the range $N_{\text{SN}}/M_* = (0.74\text{--}5.4) \times 10^{-3} M_\odot^{-1}$, where the uncertainty is dominated by the SFH. By combining the contribution from CC SNe, based on the wide range of SFHs, with that from SNe Ia, calculated with the best-fitting DTD, we predict that the mean present-day cosmic iron abundance is in the range $Z_{\text{Fe}} = (0.06\text{--}0.37) Z_{\text{Fe},\odot}$. We further predict that the high- z SN searches now beginning with *HST* will discover a significant number of SNe Ia at $z > 2$.

Key words: surveys – supernovae: general – cosmology: miscellaneous – cosmology: observations

1 INTRODUCTION

Supernovae (SNe) play important roles in a variety of astrophysical settings, from galaxy evolution to the metal enrichment of the interstellar medium, as catalysts of star formation, and as distance indicators. SNe are separated into two main physical classes: core-collapse SNe (CC SNe), which include all type II SNe (i.e., those objects which exhibit H lines in their spectra) and Type Ib/c SNe (i.e., spectra lacking H and with weak Si and S lines); and type Ia SNe (SNe Ia), which show strong Si and S, but no H, lines in their spectra (see Filippenko 1997 for a review; see Perets et al. 2010 for a possible exception). CC SNe occur in massive stars that have reached the end of their fuel cycles. Pre-explosion images have revealed directly the progenitors of some CC SNe (see Smartt 2009 for a review). In contrast, SNe Ia are thought to be the result of the thermonuclear combustion of carbon-oxygen white dwarfs (WDs) that approach the Chandrasekhar limit through mass accretion in close binary systems (see Hillebrandt & Niemeyer 2000 and Howell 2010 for reviews). Two basic routes have been suggested for the WD to grow in mass. The single-degenerate model postulates mass accretion from a main-sequence or giant companion star (Whelan & Iben 1973), while the double-degenerate (DD) model invokes the merger of two WDs (Iben & Tutukov 1984; Webbink 1984). However, there have been no unambiguous identifications of SN Ia progenitors in pre-explosion images, or of remaining companions in historical SN Ia remnants (e.g., Voss & Nelemans 2008; Roelofs et al. 2008; González Hernández et al. 2009; Kerzendorf et al. 2009). Programs that seek to determine the DD merger rate by surveying for WD binaries (Napiwotzki et al. 2004; Geier et al. 2007; Badenes et al. 2009) have yet to conclude whether this channel can account for some or all of the SN Ia rate.

One way to constrain indirectly the different SN Ia progenitor models is through their delay-time distribution (DTD) — the distribution of times between a hypothetical δ -function-like burst of star formation, and the subsequent SN Ia explosions. Different progenitor and explosion models predict different forms of the DTD (e.g., Yungelson & Livio 2000; Han & Podsiadlowski 2004; Ruiters, Belczynski, & Fryer 2009; Mennekens et al. 2010). There are various ways to estimate the DTD observationally. Mannucci et al. (2005) compared the SN Ia rate per unit mass in different types of galaxies and found that the rate in blue galaxies is a factor of 30 larger than in red galaxies. This result led to the so-called ‘ $A + B$ ’ model (Scannapieco & Bildsten 2005), which reproduces the SN rate with a term proportional (through A) to the total stellar mass of the SN host population, and a second term which is proportional (through B) to the star formation rate (SFR) of the host population. The $A + B$ model is effectively a two-time-bin approximation of the DTD.

Totani et al. (2008) compared the SN rates in elliptical galaxies in the Subaru-XMM Deep Field (SXDF) to the mean ages of their stellar populations, and deduced a power-law shape of the form $\Psi(t) \propto t^\beta$ for the DTD, with $\beta \approx -1$ in the delay-time range of 0.1–4 Gyr. Maoz et al. (2010a) compared the SN rate and the star formation histories (SFHs) of a subset of the galaxies monitored by the Lick Observatory SN Search (Leaman et al. 2010). They

reconstructed a falling DTD, with significant detections of both ‘prompt’ SNe Ia (with delays of < 200 Myr) and ‘delayed’ ones (> 2.5 Gyr). Similar results were obtained by Brandt et al. (2010), analysing the SNe Ia from the Sloan Digital Sky Survey II (SDSS-II; York et al. 2000). Maoz & Badenes (2010) compared between the SN rate in the Magellanic Clouds as inferred from SN remnants and the SFHs of their resolved stellar populations, and detected a prompt component in the DTD. Comparisons of the rates of SNe Ia and the luminosity-weighted mean ages of their host populations have been undertaken by Aubourg et al. (2008); Raskin et al. (2009); Cooper, Newman, & Yan (2009); and Yasuda & Fukugita (2010).

Measurement of SN rates versus redshift in galaxy clusters has provided another powerful probe of the DTD. Cluster SFHs are relatively simple, and thus the form of the DTD is obtainable almost directly from the SN rate as a function of cosmic time. Furthermore, the deep gravitational potentials mean that the total metal content of clusters, as quantified by optical and X-ray measurements, provide a record of the time-integrated contributions, and hence numbers, of SNe over the cluster histories. This sets the integral of the DTD. Maoz, Sharon, & Gal-Yam (2010b) have recently compiled and analysed cluster SN rates from a number of surveys in the redshift range $0 < z < 1.5$ (Gal-Yam, Maoz, & Sharon 2002; Sharon et al. 2007, 2010; Graham et al. 2008; Mannucci et al. 2008; Dilday et al. 2010b; Barbary et al. 2010). They find that the best-fitting DTD is a power law with an index of $\beta = -1.1 \pm 0.2$ or $\beta = -1.3 \pm 0.2$, depending on the assumed value of the present-day stellar-to-iron mass ratio in clusters. Thus, a variety of recent attempts to recover the DTD, involving a range of techniques, redshifts, and environments, consistently indicate a power-law DTD with index $\beta \approx -1$ (see Maoz et al. 2010b for an intercomparison of these results).

There is, however, one approach to recover the DTD that has produced some conflicting results. The SN rate in field galaxies at cosmic time t , $R_{\text{Ia}}(t)$, is the convolution of the SFH, $S(t)$, with the DTD, $\Psi(t)$:

$$R_{\text{Ia}}(t) = \int_0^t S(t - \tau) \Psi(\tau) d\tau. \quad (1)$$

The DTD can therefore be recovered, in principle, by comparing the field SN Ia rate vs. redshift to the cosmic SFH. The cosmic SFH has been measured out to $z \approx 6$ (see, e.g., compilation in Hopkins & Beacom 2006, hereafter HB06), and several surveys have attempted to extend these measurements out to $z \approx 8$ (Verma et al. 2007; Yüksel et al. 2008, hereafter Y08; Bouwens et al. 2008; Reddy & Steidel 2009; Kistler et al. 2009; Yan et al. 2009). While all surveys observe a rise in the SFH towards $z = 1$ –2.5, to date estimates of the SFH based on the ultraviolet (UV) emission of field galaxies (e.g., Bouwens et al. 2010, hereafter B10) have produced shallower evolutions than those based on the far-infrared (IR) continuum of galaxies, (e.g., Le Floc’h et al. 2005; Rujopakarn et al. 2010). This is due to the systematic uncertainty introduced by the need to correct the observed UV luminosity for extinction by dust. A recent attempt by Oda et al. (2008, hereafter O08) to derive the cosmic SFH using CC and Ia SN rate measurements found constraints which are consistent with the latest IR-based SFH measurements.

Gal-Yam & Maoz (2004) were the first to set constraints on the DTD with this approach, based on a small sample of SNe Ia out to $z = 0.8$. A number of surveys over the past decade have measured the SN Ia rate out to $z \approx 0.2$ (Cappellaro, Evans, & Turatto 1999; Hardin et al. 2000; Pain et al. 2002; Tonry et al. 2003; Blanc et al. 2004; Botticella et al. 2008, hereafter B08; Horesh et al. 2008; Li et al. 2010a). Additional surveys, such as the SDSS (Madgwick et al. 2003; Dilday et al. 2008, 2010a) and the Supernova Legacy Survey (SNLS; Neill et al. 2006, hereafter N06, and Neill et al. 2007) have added measurements out to $z \approx 0.8$. The previously discordant measurements of the Institute for Astronomy (IfA) Deep Survey (Barris & Tonry 2006) have recently been corrected and extended to redshift $z = 1.05$ by Rodney & Tonry (2010).

Measurements of the SN rate at $z > 1$ were first realized by Dahlen et al. (2004, hereafter D04), using the *HST* Advanced Camera for Surveys (ACS) observations of the GOODS fields. Additional data were analysed in Dahlen, Strolger, & Riess (2008, hereafter D08). D04 and D08 argued that their data indicate a peak in the SN rate at $z \approx 0.8$, with a steep decline at higher redshifts. Based on this rate evolution, Strolger et al. (2004), D04 and D08 deduced a best-fitting narrow Gaussian-shaped DTD, centred at a delay time of 3.4 Gyr. Similarly, Strolger, Dahlen, & Riess (2010) adopted a unimodal, skew-normal function (see their equation 6) for the DTD, from which they inferred that the DTD should be confined to a delay-time range of 3–4 Gyr. However, analysing much of the same data, Kuznetsova et al. (2008) found that they could not distinguish between a flat SN rate at $z > 0.5$ and a decline at $z > 1$, due to the large statistical and systematic uncertainties in the *HST*/GOODS dataset. Similar attempts by Blanc & Greggio (2008) and Horiuchi & Beacom (2010) to couple between the cosmic SFH and the SN Ia rates from the above data also led to the conclusion that a broad range of DTD models could be accommodated by the data, including power-law DTDs, due to small-number statistics. In three *HST* cycles, GOODS found 53 SNe Ia, of which only 3 were in the $1.4 < z < 1.8$ range. Larger SN Ia samples are clearly needed in order to determine precise rates at these redshifts, to recover the DTD, and to compare it to other measurements.

To address this problem, in 2005 we initiated a ground-based high- z SN survey with the objective of determining the SN Ia rate at $z > 1$. Our survey is based on single-epoch discovery and classification of SNe in the Subaru Deep Field (SDF; Kashikawa et al. 2004, hereafter K04). In 2007 we presented initial results from our survey for SNe Ia out to $z = 1.6$, based on the first epoch of observations (Poznanski et al. 2007b, hereafter P07b). This first epoch produced a number of SNe Ia that was similar to that found by D04 in GOODS. The high- z rates we found were also consistent with those of D04 and D08, with similar uncertainties, but our results suggested a flat rather than a declining SN Ia rate at high redshifts.

In this paper, we present our final sample of 150 SNe, based on four SDF epochs, and derive the most precise SN Ia rates to date at $1 < z < 2$. In Section 2 we describe our observations of the SDF and spectroscopy of several of our SN host galaxies. Sections 3 and 4 detail our methods for discovering the SNe and their host galaxies. In Section 5 we classify the SN candidates into SNe Ia and CC SNe with the

SN Automatic Bayesian Classifier (SNABC) algorithm of Poznanski, Maoz, & Gal-Yam (2007a, hereafter P07a). The distribution of SNe among types and redshift bins is examined in Section 6, and corrected for biases introduced by the SNABC. We derive the SN Ia and CC SN rates in Section 7. The SN Ia rates, along with rates collected from the literature, are then used to constrain the DTD in Section 8. The best-fitting DTD is used to predict the SN Ia rate at $z > 2$ and calculate the accumulation of iron in the Universe, as a function of redshift, in Section 9. We summarize and discuss our results in Section 10. Throughout this paper we assume a Λ CDM cosmological model with parameters $\Omega_\Lambda = 0.7$, $\Omega_m = 0.3$, and $H_0 = 70 \text{ km s}^{-1} \text{ Mpc}^{-1}$. Unless noted otherwise, all magnitudes are on the AB system (Oke & Gunn 1983).

2 OBSERVATIONS AND REDUCTIONS

2.1 Imaging

The SDF ($\alpha = 13^{\text{h}}24^{\text{m}}39^{\text{s}}$, $\delta = +27^\circ29'26''$; J2000) was first imaged by K04 with the Suprime-Cam camera on the Subaru 8.2-m telescope on Mauna Kea, Hawaii. Suprime-Cam is a 5×2 mosaic of $2\text{k} \times 4\text{k}$ pixel CCDs at the prime focus of the telescope, with a field of view of $34 \times 27 \text{ arcmin}^2$, and a scale of $0.202 \text{ arcsec pixel}^{-1}$ (Miyazaki et al. 2002). K04 imaged the SDF in five broad-band filters (B , V , R , i' , and z') and two narrow-band filters ($NB816$ and $NB921$), over an area of $30 \times 37 \text{ arcmin}^2$, down to 3σ limiting magnitudes of $B = 28.45$, $V = 27.74$, $R = 27.80$, $i' = 27.43$, $z' = 26.62$, $NB816 = 26.63$, and $NB921 = 26.54$ (5σ limits of $B = 27.87$, $V = 27.15$, $R = 27.24$, $i' = 27.01$, $z' = 26.06$, $NB816 = 26.24$, and $NB921 = 26.07$), as measured in circular apertures having radii of 1 arcsec. See K04 for details of those observations. This initial epoch of optical observations is denoted here as ‘epoch 1.’

In our analysis, we also make use of additional existing data on the SDF, particularly for estimating the properties of the galaxies hosting the SNe we find. Near-infrared (NIR) photometry, in J and K , was obtained with the Wide-Field Camera on the United Kingdom Infrared Telescope (UKIRT; Hayashi et al. 2009; Motohara et al., in preparation) down to 3σ limiting magnitudes of $J = 24.67$ and $K = 25.07$ in apertures with radii of 1 arcsec (5σ limits of $J = 24.33$ and $K = 24.52 \text{ mag}$). While the K -band data cover the same area of the SDF as the optical observations, the J -band data cover only ~ 40 per cent of the field. UV observations of the SDF were obtained by the *Galaxy Evolution Explorer* (GALEX), with total exposures of 81 ks in the far-UV (FUV) band ($\lambda \approx 1530 \text{ \AA}$) and 161 ks in the near-UV (NUV) band ($\lambda \approx 2270 \text{ \AA}$). These integration times result in 3σ limiting magnitudes of 26.42 and 26.49 in the (FUV) and (NUV) bands, respectively, in apertures with radii of 7.5 arcsec (or 5σ limits of 25.86 and 25.93 mag).

We reimaged the field on four separate epochs (UT dates are used throughout this paper): 2005 March 5 and 6 (epoch 2, analysed by P07b); 2007 February 12–15 (epoch 3); 2007 May 15 and 16 (epoch 4); and 2008 June 1–4 (epoch 5). During epochs consisting of two nights, the SDF was observed during most of the night. On the epochs that were spread over four nights, either the first or the second half

Table 1. Summary of optical imaging data for epochs 2 through 5

Epoch	Band	Exp. [s]	Seeing [arcsec]	3σ m_{lim} ^a [mag]	5σ m_{lim} ^b [mag]	m_0 ^c [mag/count]	UT Date
2	<i>R</i>	7,920	1.06	27.18	26.63	33.93	2005 Mar. 5/6
	<i>i'</i>	10,800	0.99	27.00	26.45	33.99	2005 Mar. 5/6
	<i>z'</i>	18,240	1.03	26.33	25.77	32.92	2005 Mar. 5/6
3	<i>R</i>	11,460	0.79	27.98	27.43	34.08	2007 Feb. 12/13/14/15
	<i>i'</i>	15,000	0.80	27.79	27.24	34.11	2007 Feb. 12/13/14/15
	<i>z'</i>	27,240	0.85	26.90	26.35	33.01	2007 Feb. 12/13/14/15
4	<i>R</i>	8,220	0.90	27.36	26.80	33.14	2007 May 15/16
	<i>i'</i>	7,960	0.84	27.17	26.62	33.16	2007 May 15/16
	<i>z'</i>	17,150	0.73	26.86	26.30	31.87	2007 May 15/16
5	<i>R</i>	10,550	0.83	27.70	27.14	34.00	2008 Jun. 1/2/3/4
	<i>i'</i>	12,960	0.81	27.50	26.94	34.06	2008 Jun. 1/2/3/4
	<i>z'</i>	23,500	0.73	27.21	26.66	32.99	2008 Jun. 1/2/3/4

^a 3σ limiting magnitude, within a circular aperture having a radius the size of the image's seeing FWHM.

^b 5σ limiting magnitude.

^cMagnitude zero point, i.e., the magnitude of a source in the image with 1 count ($2.6 e^-$).

of each night was dedicated to the SDF program. In either case, we consider the consecutive nights to be a single epoch, whose nightly images can be coadded, given the longer time scales on which SNe evolve at the redshifts we probe. On all occasions, we imaged the field in the three reddest Suprime-Cam broad bands: *R*, *i'*, and *z'*. These filters, which probe the rest-frame blue emission of SNe at $z = 1-2$, are the most suitable for discovering and classifying such SNe (e.g., Poznanski et al. 2002; Gal-Yam et al. 2004; Riess et al. 2004). We followed a dithering pattern similar to the one described by K04. Table 1 lists the exposure times, average seeing, and limiting magnitudes in each band, for epochs 2 through 5. In general, the average seeing for each night ranged between 0.7 and 1 arcsec full width at half-maximum intensity (FWHM).

We reduced the Subaru observations with the Suprime-Cam pipeline *SDFRED* (Yagi et al. 2002; Ouchi et al. 2004). Briefly, the individual frames were overscan subtracted, flat fielded using superflats, distortion corrected, sky subtracted, registered, and combined. In contrast to K04 and P07b, we did not apply point-spread function (PSF) degradation on the new images, since it reduces the frame depth. The combined image was then matched to the *i'*-band image from K04 by using the *astrometric*¹ code to find the astrometric correction, and the IRAF² (Tody 1986) task *wregister* to register the two images. The photometric calibration of the images from epoch 1 was done by K04, achieving a precision for the zero points of ~ 0.05 mag (see section 4.2 of K04). We calibrated our images relative to epoch 1 by comparing the photometry of all the objects detected with SExtractor (Bertin & Arnouts 1996) in both epochs. The mean of the differences between the two measurements was taken to be the difference in zero points.

In order to create a reference image to be compared to each epoch, the images from all the other epochs were

scaled, weighted according to their depth, and stacked using the IRAF task *imcombine*. The stacking process included a sigma-clipping procedure that excluded any transient or highly variable objects from the resulting summed image. Four ‘master’ images were created in this fashion, for each search epoch, where each such image is composed of all other epochs, except the search epoch in question. These master images proved deeper and sharper than the original epoch-1 images used by P07b as reference images for the subtraction process. For example, the epoch-5 master image has a 3σ limiting magnitude of $z' = 27.01$, as measured in an aperture having a radius the size of the image’s PSF FWHM of 0.96 arcsec, and is the deepest of the master images. As discussed in Section 3.1 below, the use of the new master images as reference images resulted in the discovery of SNe in epoch 2 that went undiscovered by P07b.

We performed PSF matching, scaling and image subtraction between the target and reference images in each Subaru epoch in all bands, using the software HOTPANTS³, an implementation of the ISIS algorithm of Alard & Lupton (1998) for image subtraction (as described in Becker et al. 2004). Briefly, HOTPANTS divides the images into a predetermined number of regions, and in each region finds the convolution kernel necessary to match the PSF of one image to that of the other. HOTPANTS is similar to ISIS, which was used by P07b, but allows more control over the subtraction process. For example, each region of the image is subdivided into stamps and substamps, where the substamps are centred on astronomical objects. The kernel is then computed for each substamp, producing a distribution of values used to sigma-clip outliers, thus ensuring a more accurate determination of the kernel in each stamp, and ultimately a better mapping of the spatial variations of the kernel across the image. We also made use of the software’s ability to mask saturated pixels, which vastly reduced the number of residuals in the difference images.

As a consequence of the dithering, the final images have a field of view of 0.31 deg^2 ; however, due to the different ef-

¹ <http://www.na.astro.it/~radovich>

² IRAF is distributed by the National Optical Astronomy Observatories, which are operated by the Association of Universities for Research in Astronomy, Inc., under cooperative agreement with the National Science Foundation (NSF).

³ <http://www.astro.washington.edu/users/becker/hotpants.html>

fective exposures in the fringes of the field, a substantial region along the edges suffers from a significantly lower signal-to-noise ratio (S/N). We therefore crop the edges of the difference image, ending with a total subtraction area of 0.25 deg².

2.2 Spectroscopy

As detailed in section 2.2 of P07b, we obtained spectra of some of the SN host galaxies from epoch 2, together with several hundred random galaxies in the SDF, using the Low-Resolution Imaging Spectrometer (LRIS; Oke et al. 1995) on the Keck I 10-m telescope, and the Deep Imaging Multi-Object Spectrograph (DEIMOS; Faber et al. 2003) on the Keck II 10-m telescope.

In addition to the SN host spectra published by P07b, we obtained spectra of 7 additional SN host galaxies. These spectra were obtained during observations carried out on the night of 2010 February 15 with DEIMOS on the Keck II telescope. The single mask utilized for these observations contained 16 SN host galaxies, as well as the positions of tens of filler galaxies. The mask was observed for a total of 3×30 min. We used the 600 line mm⁻¹ grating, with the GG455 order-blocking filter and a wavelength range of $\sim 4400\text{--}9600$ Å, with the exact limits depending on each individual spectrum.

The 600 line mm⁻¹ grating yields a FWHM intensity resolution of ~ 3 Å, or ~ 120 km s⁻¹, at 7500 Å. This resolution is sufficient to resolve many night-sky lines and the [O II] $\lambda\lambda 3726, 3729$ doublet. By resolving night-sky lines, one can find emission lines in the reddest part of the spectrum, where sky lines are blended in low-resolution spectra. Furthermore, by resolving the [O II] doublet, we can confidently identify an object's redshift, even with only a single line.

The DEIMOS data were reduced using a modified version of the DEEP2 data-reduction pipeline⁴, which bias corrects, flattens, rectifies, and sky subtracts the data before extracting a spectrum (Foley et al. 2007). The wavelength solutions were derived by low-order polynomial fits to the lamp spectral lines, and shifted to match night-sky lines at the positions of the objects. Finally, the spectra were flux calibrated by scaling them to the mean flux in the *R* and *i'* bands. Consequently, the displayed continuum spectral shape is not precisely calibrated. In any event, the continuum emission of the host galaxies is weak and noisy, and therefore we rely on spectral lines alone for redshift identification.

3 SUPERNOVA CANDIDATES

In this Section we describe the methods by which we have discovered the SN candidates in our sample, derive the detection efficiency of the survey, and measure the photometric and astrometric properties of the candidates and their uncertainties. We have discovered a total of 163 transient objects, of which 150 are most likely SNe. The luminosities of the transients, inferred from their measured photometry

and the redshifts of their associated host galaxies (as derived in Section 4.2, below), lead us to conclude that these 150 events are SNe. In Section 3.1 we describe the criteria according to which the transients were chosen, culling random noise peaks, image subtraction artefacts, and previously known active galactic nuclei (AGNs). We calculate the probability of contamination by flaring Galactic M dwarfs and unknown AGNs in Section 4.1. The probable contamination by AGNs is compared with the number of actual possible AGNs among the candidates in Section 5.1. In Section 4.1 we also calculate the probability of a chance association between a transient object and its surrounding galaxies.

Since our survey classifies SNe based on single-epoch observations without spectroscopic follow-up observations, the SNe we discover do not satisfy the International Astronomical Union's criteria for a 'standard' designation. As in P07b, we will continue to use the following naming conventions. We denote the SNe from epochs 2 through 5 respectively as 'SNSDF0503.XX,' 'SNSDF0702.XX,' 'SNSDF0705.XX,' and 'SNSDF0806.XX,' with the first two digits denoting the year, the next two digits the month, and XX being a serial number ordered according to the SN *z'*-band apparent magnitude. The respective host galaxies are referred to as 'hSDF0503.XX,' 'hSDF0702.XX,' 'hSDF0705.XX,' and 'hSDF0806.XX.'

3.1 Candidate selection

The *z'*-band difference image obtained with HOTPANTS was scanned with SExtractor to search for variable objects. SExtractor was set to identify and extract all objects which had at least 6 connected pixels with flux 3σ above the local background level. Morokuma et al. (in preparation) conducted a study of the various variable objects in epoch 1, as a part of which they identified nearly a thousand AGNs in the SDF based on their long-term *i'*-band variability. In our survey, these galaxies were therefore ignored. These galaxies still constitute fewer than 1 per cent of all galaxies in the SDF, and therefore this exclusion will have negligible effect on our SN survey.

In order to reject other non-SN events, the remaining variable candidates were examined as follows.

- (i) Of the objects identified by SExtractor, we rejected all those which showed suspect residual shapes, indicative of a subtraction artefact.
- (ii) We compared two *z'*-band difference images of the same field. The main difference image was obtained by allowing HOTPANTS to calculate the convolution kernel for the subtraction over the entire image. A second difference image was obtained by forcing HOTPANTS to break the image into four subregions, and calculate the convolution kernel in each one. This second difference image was generally less clean than the first, but allowed for the rejection of subtraction artefacts in the main difference image, as not all of those would be reproduced in the second subtraction process.
- (iii) We compared the main *z'*-band difference image in a certain epoch with difference images of the other epochs in order to identify and reject AGNs that were not already rejected based on the catalogue of Morokuma et al. (in prepa-

⁴ <http://astro.berkeley.edu/~cooper/deep/spec2d/>

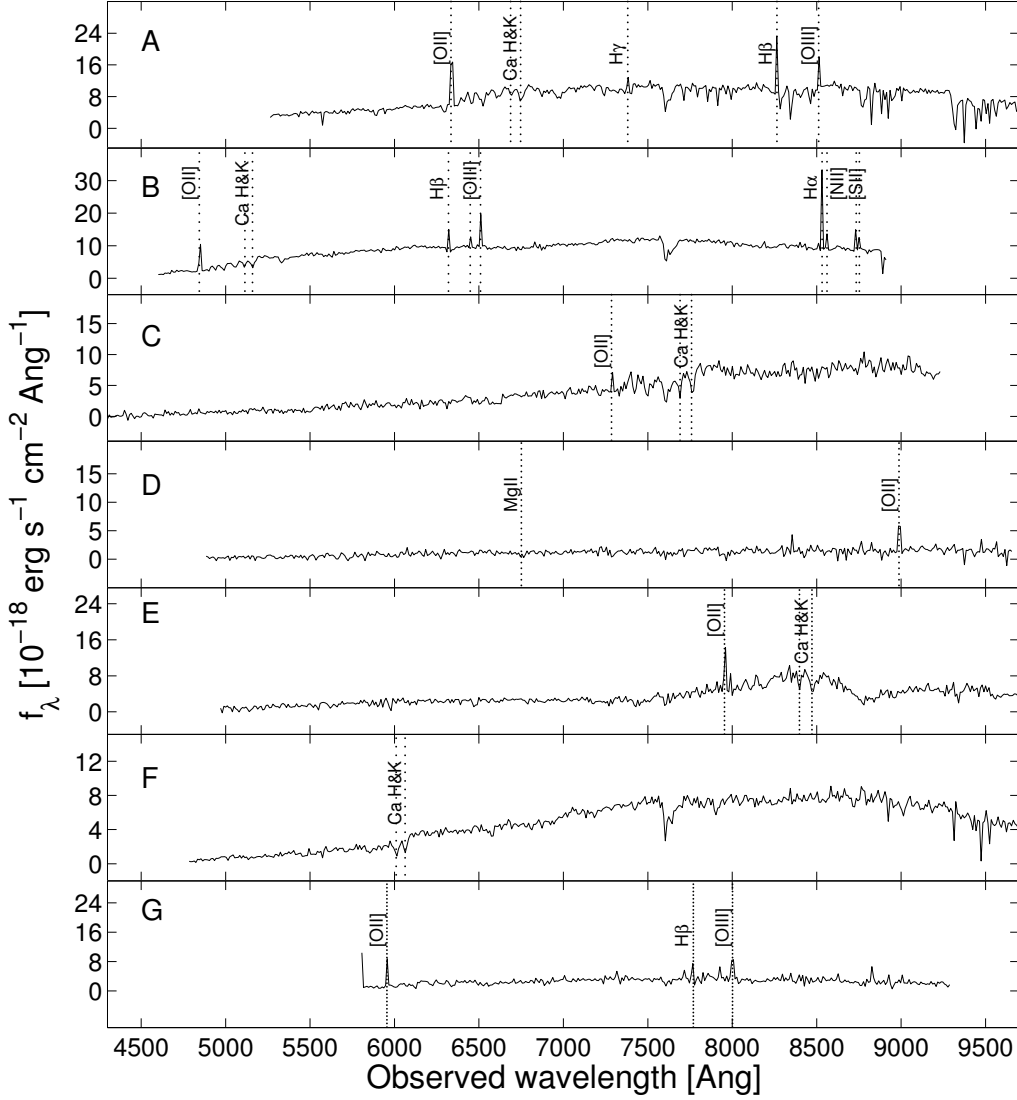


Figure 1. SN host-galaxy spectra from the 2010 February 15 Keck DEIMOS observations, with the prominent emission and absorption features marked. The spectra have been rebinned into 10 \AA bins. (a) hSDF0702.03, $z = 0.70$; (b) hSDF0702.21, $z = 0.30$; (c) hSDF0702.23, $z = 0.96$; (d) hSDF0705.18, $z = 1.41$; (e) hSDF0806.48, $z = 1.13$; (f) hSDF0806.54, $z = 0.53$; and (g) hSDF0806.55, $z = 0.60$.

ration), or other objects that exhibited variability over a large stretch of time.

(iv) In order to further reject subtraction artefacts, we stacked the exposures in each epoch into two subepoch images, where each subepoch was composed of half of the observation nights. These images were then used to obtain new difference images which we compared with the main z' -band images. As in the previous steps, objects which appeared in the main difference image, but not in the subepoch difference images, were rejected. We note that solar-system objects were already eliminated in the nightly averaging, since even as far as 30 AU (Stern & Colwell 1997) a Kuiper Belt object would move due to the Earth's motion by ~ 40 arcsec, or 200 pixels, in the course of an 8-hour night.

(v) For every candidate found in the z' band, difference images in the R and i' bands were also examined, and objects which showed suspect residual shapes were rejected. We note that no candidate was rejected because of a nondetection in the R or i' bands, since at least some high- z SNe are expected to be very faint or undetected in the observed-frame R and i' bands.

(vi) Finally, for each SN candidate, we derived the local S/N by dividing the SN counts in an aperture of 1 arcsec radius (before application of an aperture correction) by the standard deviation of the total counts in tens of identical apertures centred on surrounding blank regions. SN candidates which had a S/N smaller than 3 were rejected as probable noise peaks.

We note that steps (ii) and (iii) are selection criteria additional to those followed by P07b.

In order to apply our new criteria uniformly to the full SN survey, we resurveyed epoch 2. Of the 33 SNe found by P07b, 28 were recovered. The SN candidates listed in P07b as SNSDF0503.27, SNSDF0503.33, and SNSDF0503.40 were not detected by SExtractor, because the S/N was too low. While the first two SN candidates listed above appear in the difference images, we do not detect the third one in our renewed analysis. SNSDF0503.29 was detected by SExtractor, but whereas in the main difference image it appears as a point source, in the secondary difference image it is extended, and the position of its centre is offset by ~ 0.35 arcsec. SNSDF0503.32 was not detected by SExtractor, and while it appears in the main difference image, it is absent from the secondary difference image. Thus, with our improved reference images and image subtraction procedures, these events from P07b do not pass our current selection criteria.

On the other hand, we have discovered 8 new SN candidates in epoch 2, not reported by P07b. In this work, these SN candidates are listed as SNSDF0503.06, SNSDF0503.16, SNSDF0503.19, SNSDF0503.27, SNSDF0503.31, SNSDF0503.32, SNSDF0503.33, and SNSDF0503.34. The differences between the P07b sample and the present sample are due to two reasons: (a) the use of HOTPANTS in the current work, which provides cleaner subtractions than ISIS, and (b) the use of deeper z' -band master images with better image quality, instead of the shallower epoch-1 z' -band image, as references. In any event, the list of epoch-2 SNe that we report in Table 7 supersedes the one presented by P07b.

3.2 Detection efficiency simulation

In our survey, SNe may be missed as a result of many effects, including imperfect subtractions, noise fluctuations, and human error. In order to quantify these systematic effects, we measure our detection efficiency by blindly planting artificial point sources, which match the SN population in our survey as closely as possible, in the presubtraction z' -band images, and then discovering them along with the real SNe. The simulated SN sample was constructed as detailed in section 3.2 of P07b. Our resulting efficiency as a function of magnitude, in each epoch, can be seen in Fig. 2. We follow Sharon et al. (2007) and fit the following function to the data:

$$\eta(m; m_{1/2}, s_1, s_2) = \begin{cases} \left(1 + e^{\frac{m - m_{1/2}}{s_1}}\right)^{-1}, & m \leq m_{1/2} \\ \left(1 + e^{\frac{m - m_{1/2}}{s_2}}\right)^{-1}, & m > m_{1/2}, \end{cases} \quad (2)$$

where m is the z' -band magnitude of the fake SNe, $m_{1/2}$ is the magnitude at which the efficiency drops to 0.5, and s_1 and s_2 determine the range over which the efficiency drops from 1 to 0.5, and from 0.5 to 0, respectively.

3.3 Supernova sample

We have found a total of 150 SNe, with magnitudes in the range $z' = 22.9$ to $z' = 26.7$. Table 7 lists the SNe and

their properties. Apart from these 150 SNe, we detect several tens of candidates at fainter magnitudes, as we would expect based on our efficiency simulations, but these are all objects with $S/N < 3$. While some of these objects may be SNe, an unknown number of them could be false positives, such as subtraction artefacts or random noise peaks. We therefore limit our sample to $z' < 26.3$, $z' < 26.6$, $z' < 26.4$, and $z' < 26.7$ mag for epochs 2 through 5, respectively. These are the values of $m_{1/2}$ in each epoch.

Using SExtractor, we have performed aperture photometry of the SNe in the R , i' and z' difference images within fixed 1-arcsec-radius circular apertures. To estimate the aperture correction and photometric uncertainty, we measured the magnitudes of ~ 600 simulated point sources, ranging in brightness from 23 to 28 mag, planted in a $4k \times 4k$ pixel subframe of the SDF R -, i' -, and z' -band images. We took the difference between the average of the magnitude in each bin and the true magnitude as the required aperture correction, and the standard deviation in each magnitude bin to be the minimum photometric statistical error for objects of that magnitude. For example, the mean aperture correction for the epoch-2 z' -band image was 0.2 mag (i.e., due to aperture losses, the measured photometry was 0.2 mag too faint) and the standard deviation ranged from 0.03 to 0.29 mag from the brightest to the faintest artificial sources, respectively. The adopted uncertainty for each SN was taken to be the larger among the uncertainty computed by SExtractor and the statistical uncertainty for the given magnitude bin from the simulations.

We also measured the offset of each SN from its host galaxy. To estimate the uncertainty of the offset, $\sim 12,000$ simulated point sources, divided into magnitude bins of width 0.3 mag, were planted in the z' -band image of each epoch. We then measured their locations, in both the original image and the z' -band difference image, using SExtractor, and took the mean of the location residuals in each bin as an estimate of the uncertainty of the object's location. This uncertainty was added, in quadrature, to the uncertainty in the location of the SN host galaxy. The real SN offsets ranged between 0 and 3.61 arcsec, and the uncertainties ranged between 0.02 and 0.16 arcsec, with the centres of brighter sources being, of course, better localized.

4 SUPERNOVA HOST GALAXIES

In this Section, we determine the host galaxy of each SN and then measure its properties. The SN host galaxies, including their photometry in all available bands, are presented in Table 8.

4.1 Identification and photometry

The SN host galaxies were chosen to be the closest galaxies, in units of those galaxies' half-light radii, as measured with SExtractor in the i' band. A small number of SNe had several possible hosts. To choose between them we measured the photometric redshift (photo- z) of each host. If the different hosts were found to be at the same redshift, that redshift was adopted for the SN as well. If, on the other hand, the different hosts were found to lie at different redshifts, we computed the likelihood of a SN of the type, as

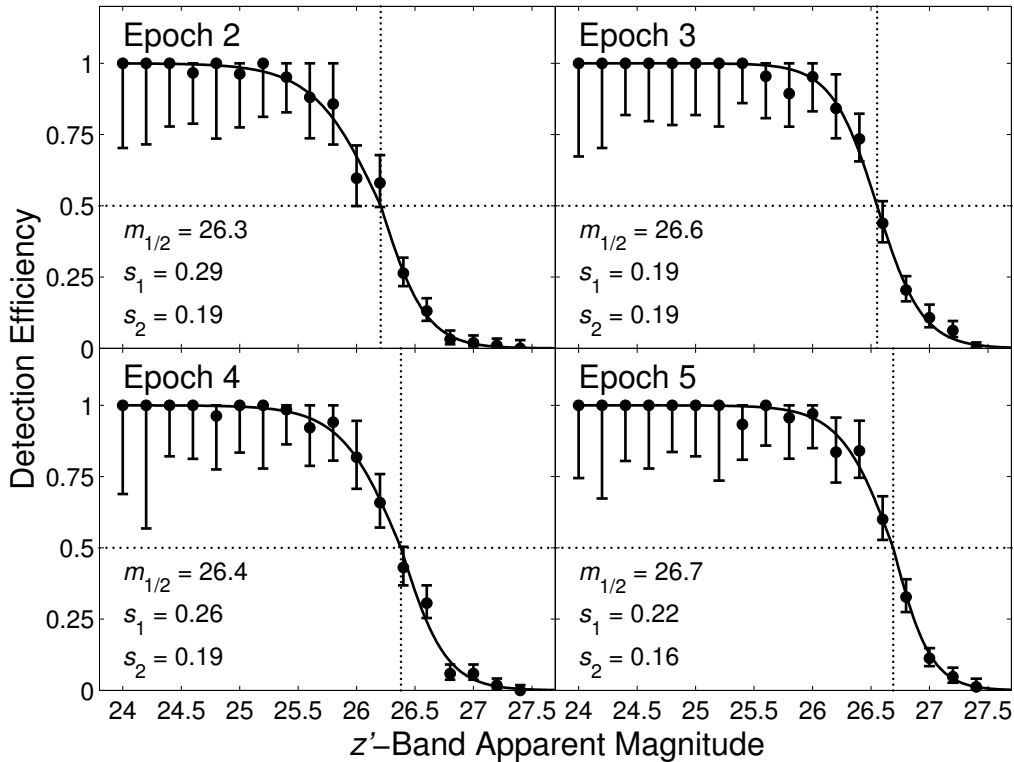


Figure 2. Fraction of simulated SNe recovered as a function of z' -band magnitude. Error bars indicate 1σ binomial uncertainties. The dotted lines mark the 50 per cent efficiency mark.

classified by SNABC, at those different redshifts being observed at the magnitude measured. In this manner we were able to eliminate unlikely hosts.

Using SExtractor, we measured the Petrosian (1976) magnitude of the host galaxies in the seven optical bands of epoch 1. We chose Petrosian photometry, since it measures the flux of resolved objects within a given fraction of the object’s light profile, thus enabling one to compare between measurements taken in different filters. The resulting catalogue was cross-matched with the *J* and *K* catalogues. Additionally, for each galaxy we checked the corresponding location in the *GALEX FUV* and *NUV* background-subtracted images. Since the *GALEX* PSF is much larger than that of Subaru and UKIRT, most of our galaxies appear as point sources, making it impossible to measure Petrosian magnitudes; hence, any measurement within any aperture would not capture the same percentage of light as in the optical and NIR bands. Furthermore, owing to the density of sources in the SDF and the size of the *GALEX* PSF, in many cases it proved impossible to determine which source in the optical image was associated with the UV signal. In those cases where we could associate nondetections in the UV bands unambiguously with our host galaxies, we added the limiting magnitudes in the relevant UV bands to the catalogue. In Section 4.2 we detail how we combined these limiting magnitudes with the optical and NIR data to compute the redshifts of the SN host galaxies. As with the SN photometry, for the host photometry we estimated the uncertainty in each magnitude bin using artificial sources with galac-

tic profiles (created with the IRAF routine *gallist*) that we planted in the images.

To test whether any of our chosen host galaxies are merely chance associations, we counted the fractions of the total imaged SDF area that are within 0.1-light-radius-wide annuli of all the galaxies detected in the field. From this we conclude that, among the 110 SNe within ≤ 0.5 light radii of their chosen hosts, < 1 SN is expected to be a chance association. These 110 SNe include all 12 SNe in the $1.5 < z < 2.0$ range, and 24 of the 26 SNe in the $1.0 < z < 1.5$ range. At larger host-SN separations, 23, 6, and 1 of our SNe are found within 0.5–1.0, 1.0–1.5, and 1.5–2.0 light radii of their host galaxies, respectively. Among these events, we expect 6, 3, and < 1 (respectively) to be chance associations. However, 28 of these 30 large-separation events are at $z < 1$. Thus, while some fraction of our $z < 1$ rate may be due to contamination by chance associations, we estimate that our $1.0 < z < 1.5$ rate is affected by such contamination at only the few-percent level, and the $1.5 < z < 2.0$ negligibly so.

In P07b we found that, assuming a Sersic (1968) model for the galaxy radial profile between $n = 4$ (de Vaucouleurs 1948 law; Peng et al. 2002) and $n = 1$ (exponential disk; Freeman 1970; Peng et al. 2002), between 91 and 99.99 per cent of the light (respectively) falls within 6 half-light radii of the galaxy’s centre. Ten of our SNe have no visible host galaxies within this distance, and so we label them ‘hostless’ (namely SNSDF0503.14, SNSDF0503.18, SNSDF0702.06, SNSDF0705.20, SNSDF0705.21, SNSDF0705.24, SNSDF0806.04,

SNSDF0806.30, SNSDF0806.49, and SNSDF0806.53). The probable host galaxy of SNSDF0806.51 appears exclusively in the B and R bands of epoch 1. Given that our photometric redshift estimate requires at least three photometric bands for its calculation, and that even the B and R detections are barely above the limiting magnitudes in those bands, we treat this SN as hostless as well. The most probable explanation is that these SNe occurred in galaxies fainter than the limiting magnitudes in all the photometric bands of epoch 1.

Other possibilities to consider are that these candidates are high- z AGNs or flaring Galactic M dwarfs. The fact that these hostless SN candidates are detected in only a single epoch over a period of 3 years argues against the AGN option. Of the ~ 460 AGNs in the catalogue of Morokuma et al. (in preparation), < 1 per cent could have been mistaken as transients appearing in only one epoch. 50 of the SNe in our sample lie within 0.2 arcsec (or 1 pixel) of their respective host-galaxy nuclei, and so might be AGNs. Together with the above 11 hostless SNe, the predicted number of contaminating AGNs in our sample is ≈ 0.6 . The Poisson probability of having at least one AGN in the sample is then ≈ 30 per cent, which is consistent with having found one such object. The probability of finding more than 2 such objects drops to ≈ 8 per cent (see SNSDF0705.17 in Section 5.1.4 and SNSDF0705.30 in Section 5.1.6).

As to the second possibility, M-dwarf optical flares consist of a fast rise followed by a decay lasting typically of order an hour or less, with the distribution of flare durations steeply falling at longer durations (Walkowicz et al. 2010). The longest known flares last ~ 10 hrs (Kowalski et al. 2010), and these constitute < 1 per cent of all flares (E. Hilton, S. Hawley, private communication). With such variation timescales, M-star flare events would be filtered out in our nightly image averaging, or would at least show a decline between consecutive half-night averages. None of the hostless candidates show such a decline. We note, further, that flaring activity is limited to the younger M dwarfs in the Milky Way disk that are within a height of $Z < 300$ pc above the disk. Activity in older dwarfs, which have had time to be scattered to larger heights, is exceedingly rare (West et al. 2008; Kowalski et al. 2009; Walkowicz et al. 2010). Any M dwarfs below the SDF detection limits in quiescence, and that had flared into visibility during our observations, would necessarily be at distances $\gtrsim 50$ kpc, i.e., they would belong to the Galactic halo, and hence would be even older and less active than the $Z > 300$ pc disk stars. We therefore deem it highly unlikely that any of our hostless SN candidates are optical flares of Galactic M dwarfs.

4.2 Host redshifts

From our spectroscopy, detailed in Section 2.2, we derived spectroscopic redshift (spec- z) for 24 of the SN host galaxies. Of these 24 SN host galaxies, hSDF0705.18 has the highest spec- z , at $z = 1.412$. The seven new spectra obtained on 2010 February 15 appear in Fig. 1. For the majority of our SN host galaxies, which are too faint for spectroscopy, we derive photometric redshifts, as in P07b, using the Zurich Extragalactic Bayesian Redshift Analyzer (ZEBRA; Feldmann et al. 2006). We calibrated ZEBRA in the manner described by P07b, but with a larger training set of 431 galaxies, of

which 150 are in the range $1 < z < 2$. This training set was made up of 123 galaxies imaged in the Keck runs detailed by P07b, along with data from other surveys that had been conducted in the SDF (e.g., Kashikawa et al. 2003, 2006; Shimasaku et al. 2006; and a new sample obtained by N. Kashikawa in 2008 with DEIMOS on the Keck II telescope).

Since ZEBRA does not, at the moment, offer an adequate treatment of upper limits, but rather treats them as any other photometry measurement, we decided (at the suggestion of R. Feldmann, private communication) to halve the 1σ FUV and NUV flux limits, and treat them as measurements with relative uncertainties of 100 per cent, thus requiring ZEBRA's fit to pass through the region $[0, f_{1\sigma}]$. If no *GALEX* signal existed that could be clearly associated with the optical galaxy, we used the UV flux limit (as described above) as an extra band in the ZEBRA fit, thus constraining the SEDs to those with fluxes lower than the UV flux limit. If, on the other hand, there was a *GALEX* detection, but due to the large *GALEX* PSF we could not clearly associate the UV signal with the optical SN host galaxy, we did not use the *GALEX* data at all. For larger samples, where more galaxies have clear signals in the UV, one could treat the UV signal as a lower limit, in similar fashion to our use of nondetections as upper limits.

Fig. 3 displays the ZEBRA photo- z values for our training-set galaxies, compared to their spec- z values. The training set of 431 galaxies has a root-mean square (rms) scatter of $\sigma_{\Delta z}/(1 + z_s) = 0.065$ (where $\Delta z = z_s - z_p$) in the range $0 < z_p < 2$. This is a marked improvement over that of P07b, $\sigma_{\Delta z}/(1 + z_s) = 0.08$, for 296 galaxies in the range $0 < z_p < 1.8$ and after rejection of five 4σ outliers. We attribute this improvement to our enlarged training set and the addition of photometry in the UV and NIR, and posit that with deeper imaging in the NIR, over the entire area of the SDF, the dispersion would have been even lower. The rms scatter for our 24 SN host galaxies is smaller: $\sigma_{\Delta z}/(1 + z_s) = 0.028$.

Of the various end products computed by ZEBRA, we use the redshift probability distribution function (z -PDF) of each SN host galaxy that results from marginalizing the full posterior distribution over all templates. In this manner the uncertainties in the determination of the photo- z are propagated into the classification stage. While most of the z -PDFs display a single, narrow peak, some are more structured, a result of degeneracies between the different combinations of redshifts and normalization constants (i.e., a certain galaxy may fit the same template if it is bright and distant, or if it is faint and nearby) or of a dearth of information. For example, the optical continuum shape of late-type galaxies can be approximated with a power law, and so its shape is weakly affected by redshift (see, e.g., Fig. 7). In such cases the UV data can be useful; a clear signal (whether a detection or a nondetection) in the NUV band would decide among the redshift values. In order to take the uncertainty introduced by the shape of the z -PDFs into account, we use the full z -PDFs in the classification stage (see Section 5).

To each z -PDF we fit a Gaussian and compute the statistic $w = w_z/(1 + z)$, where w_z is the standard deviation of the Gaussian and z is the redshift assigned by ZEBRA. Fully 82 per cent of our SN hosts have z -PDF widths $w < 0.05$, and only 7 per cent have $w > 0.2$. For 23 of the 24 SN host galaxies with spectral redshifts,

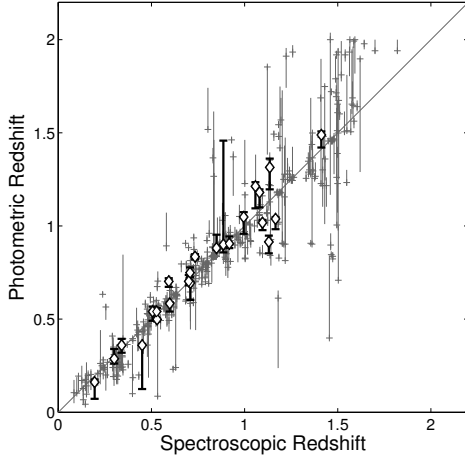


Figure 3. Comparison of the photometric redshifts derived with ZEBRA and the corresponding spectroscopic redshifts for the 431 galaxies in our training set (grey crosses) and for 24 SN host galaxies (empty diamonds). Error bars are the 1σ confidence limits from the z -PDF of each galaxy. The rms scatter of the data is $\sigma_{\Delta z/(1+z_s)} = 0.065$ for the training set and $\sigma_{\Delta z/(1+z_s)} = 0.028$ for the SN host galaxies.

the spec- z and photo- z values are almost identical, with $\Delta z/(1+z) < 0.08$, while for hSDF0503.24 the difference is only $\Delta z/(1+z) = 0.10$. For these galaxies we do not take the z -PDF computed by ZEBRA as input for the SNABC, but rather use a Gaussian z -PDF centred on that galaxy’s spec- z , with a width $w_z = 0.01$. For the 11 hostless SNe, we use a z -PDF which is the sum of the z -PDFs of all the other host galaxies. A different composite z -PDF, the average of the z -PDFs of all the galaxies in the SDF, was also tested for these SNe, and produced the same results. Given the resulting redshifts, the host galaxies of the hostless SNe would have to be fainter than between -15.8 and -17.0 to be undetected in the i' -band master images. This is consistent with these SNe having occurred in low luminosity dwarf galaxies (see, e.g., Arcavi et al. 2010).

5 SUPERNOVA CLASSIFICATION

We classify our SNe into SNe Ia and CC SNe using the SNABC algorithm of P07a. Briefly, the SNABC receives as input the photometry and z -PDF of a SN candidate. Using the above inputs, the SNABC then compares the colours of the SN candidate to the synthetic colours derived from a set of SN spectral templates of different types, ages, redshifts, host-galaxy and Galactic extinctions (based on the spectral templates of Nugent, Kim, & Perlmutter 2002, hereafter N02),⁵ and to the z' -band luminosity functions (LFs) of the different SN types. In this work we used the LFs quoted by B08 for type Ia and II-P SNe, the LF measured by Drout et al. (2010) for Ib/c SNe, and the LF measured by Kiewe et al. (2010) for type IIn SNe. Drout et al. (2010) measured peak magnitudes of $M_R = -17.9 \pm 0.9$ for SNe Ib

Table 2. SN luminosity functions, presented as absolute magnitudes (Vega) at maximum light, and Gaussian width.

Type	M_B	σ	Source
Ia	$M_B = -19.37$	0.47	Wang et al. (2006)
II-P	$M_B = -16.98$	1.00	Richardson et al. (2002)
Ib/c	$M_R = -18.20$	0.90	Drout et al. (2010)
IIn	$M_V = -18.40$	1.00	Kiewe et al. (2010)

and $M_R = -18.3 \pm 0.6$ for SNe Ic. We take the weighted average of these magnitudes and get $M_R = -18.2 \pm 0.9$ mag. Based on the N02 spectral template for SNe Ib/c, we apply a colour correction of $(B - R) = 0.6$ and arrive at $M_B = -17.6 \pm 0.9$ for SNe Ib/c. In a similar vein, we apply a colour correction of $(B - V) = -0.15$ to the LF measured by Kiewe et al. (2010) for SNe IIn, and arrive at a peak magnitude of $M_B = -18.55 \pm 1.00$. The LFs and their sources are listed in Table 2.

The SNABC computes the likelihood of each comparison, and then marginalizes over age, redshift, and extinction to arrive at the ‘evidence’ that the candidate is of a certain type: $E(\text{Ia})$ and $E(\text{CC})$. The evidence is then used to derive the probability that the candidate is either a SN Ia or CC SN, according to

$$P(\text{Ia}) = \frac{E(\text{Ia})}{E(\text{Ia}) + E(\text{CC})}. \quad (3)$$

In addition to $P(\text{Ia})$, the SNABC also produces a posterior z -PDF, for each type, and a χ^2 value. This value indicates how well the SN’s colours compared with those of the best-fitting spectral template. A high χ^2 value may imply the SN is a peculiar type of SN, an AGN, or a subtraction residual which was not rejected earlier. An event is considered a SN Ia if $P(\text{Ia}) > 0.5$ (and a CC SN if $P(\text{Ia}) < 0.5$). P07a have shown that $P(\text{Ia})$ can also be viewed as a confidence estimator: the closer it is to unity (zero), the safer the classification of the candidate as a SN Ia (CC SN). P07a also found that for the sake of classification, most CC SNe resemble SNe II-P more than SNe Ia. Thus, while SN Ia classifications usually result in small χ^2 values ($\chi^2 < 1$), CC SN classifications may result in higher values, since SNe IIn or SNe Ib/c are forcefully compared to SN II-P spectral templates.

The posterior redshift assigned to each SN by the SNABC usually matches the prior redshift assigned by ZEBRA to within 5 per cent. In those cases where the difference between the two exceeds 5 per cent, we check the w statistic of that SN’s z -PDF (i.e., $w_z/(1+z)$). A large value of w implies that the z -PDF of the SN was so wide that the colours of the SN provided more information than the z -PDF itself. In those instances where $w > 0.05$ (20 of the 150 SNe in our sample), we use the posterior redshift computed by the SNABC.

Table 7 lists the SNe in our sample, along with their redshifts and classifications. Of the 150 SNe in our sample, 26 were found in the $z < 0.5$ bin, of which 5 were classified as SNe Ia and 21 as CC SNe. The $0.5 < z < 1.0$ bin contains 86 SNe, of which 50 were classified as SNe Ia and 36 as CC SNe. The $1.0 < z < 1.5$ and $1.5 < z < 2.0$ bins contain 26 and 12 SNe, respectively, all of which were classified as SNe Ia.

⁵ http://supernova.lbl.gov/~nugent/nugent_templates.html

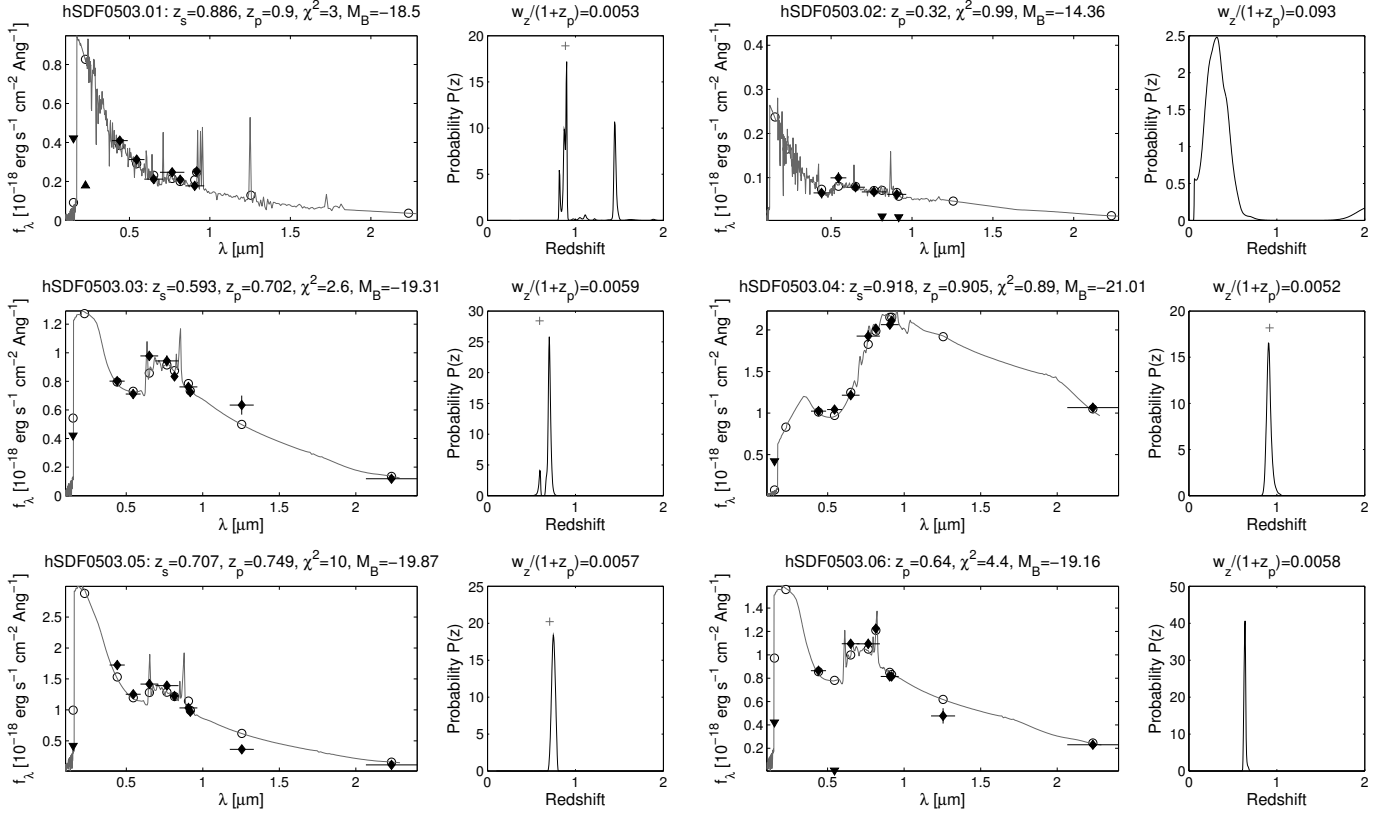


Figure 4. ZEBRA fits and resultant redshift PDFs. The left panel of every pair shows the actual photometry (filled circles), the best-fitting galaxy template (solid line), and its synthetic photometry (empty circles). The vertical error bars denote the photometric uncertainty, and the horizontal error bars show the width of the filter. The header gives the designation of the SN host galaxy, most probable photo- z (z_p), the spec- z (z_s , if such a measure exists for the specific object), the χ^2 per degree of freedom of the fit, and the absolute B -band magnitude the object would have at z_p . The right panel of every pair shows the resultant z -PDF. If a spec- z exists for the SN host galaxy, it appears as a cross. The header shows the w statistic for the z -PDF. The full figure is available in the electronic version of the paper.

Two of the 12 SNe in the $1.5 < z < 2.0$ bin have high χ^2 values, and are dealt with individually in Section 5.1.6. The remaining 10 high- z SNe Ia are shown in Fig. 5.

5.1 Notes on individual supernovae

The high χ^2 values (> 10) of some of the SNe prompted their reevaluation and, in some cases, rejection. All χ^2 values quoted are per degree of freedom.

5.1.1 SNSDF0503.25

While SNSDF0503.25 was classified as a CC SN ($P(\text{Ia}) = 0$) with a very high χ^2 value of 47.73, it is displaced from the nucleus of its spiral host by 0.63 ± 0.07 arcsec. This, together with the absence of the object from other epochs, argues against its being an AGN, though it could be a variable background quasar. Since the SNABC compares all candidates to SN Ia and SN II-P spectral templates, it is, in effect, forcefully comparing all subtypes of CC SNe to SNe II-P. This leads us to believe that this SN is, in fact, a non-SN II-P CC SN. Similar situations are encountered for SNSDF0806.05 and SNSDF0806.14.

5.1.2 SNSDF0702.01

SNSDF0702.01 was classified as a SN Ia ($P(\text{Ia}) = 1$), but with $\chi^2 = 19$. At a separation of 3.61 ± 0.02 arcsec, this $z = 0.18$ transient is well offset from the centre of its spiral host galaxy, and so precludes the possibility of an AGN (though it could be a variable background quasar). The high χ^2 value arises from this object's $R - i'$ colour, which does not fit the SN Ia template. As its absolute R -band magnitude is $M_R = -17.01$, we checked whether this could be a SN 1991bg-like SN Ia by comparing its photometry to the N02 SN 1991bg template. While the z' -band magnitude matches the template, the $R - i'$ and $i' - z'$ colours do not. Though the z' -band magnitude and $i' - z'$ colour raise the possibility that this is an early SN II-P, it is still too blue in the R band. We also checked whether the excess flux in the R band might be the result of a SN caught during shock breakout, by comparing the R -band photometry in our half-night stacks, but there was no discernible difference between the R -band flux in the first two nights and in the second two. At this point we conclude that this object is too faint and too blue to be a SN Ia, and it might be either a very blue SN II-P, or a peculiar SN of a different kind. As detailed in Section 6, since this object is at $z = 0.18$, it enters neither the SN Ia nor the CC SN rate calculations.

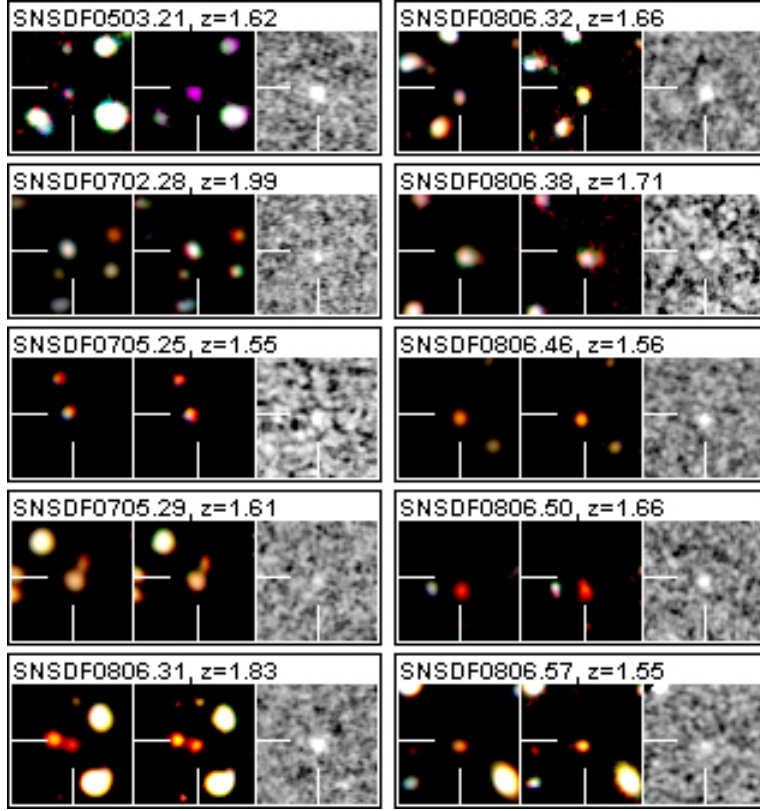


Figure 5. $1.5 < z < 2.0$ SNe Ia and host galaxies. North is up and east is left. All tiles are 10 arcsec on a side. The left-hand tiles show the SN host galaxies as imaged in epoch 1, while the center tiles display the SN host galaxy as imaged in epochs 2 through 5. R -, i' -, and z' -band images were combined to form the blue, green, and red channels (respectively) of the color composites. The right-hand tiles show the subtraction in the z' band. Whereas the stretch of the colour images differs from panel to panel in order to highlight host properties, the greyscale for all difference images is identical. The header of each panel gives the designation of the SN Ia and its redshift. Similar images of the full sample of SNe are available in the electronic version of the paper.

5.1.3 SNSDF0702.30

SNSDF0702.30 has two possible host galaxies, as shown in Fig. 6: a resolved galaxy designated hSDF0702.30a, and a compact galaxy to the NW (upper right; hSDF0702.30b). We used the software GALFIT⁶ (Peng et al. 2010) to fit and subtract the larger galaxy, thus enabling us to perform photometry of each galaxy on its own. The resulting photometry and best-fitting ZEBRA SEDs are shown in Fig. 7. Both galaxies agree well with the power-law SED of a star-forming galaxy at a high redshift (hSDF0702.30a at $z = 1.95$ with $\chi^2 = 3.5$, and hSDF0702.30b at $z = 1.72$ with $\chi^2 = 0.8$). While the fit in Fig. 7 does not utilize UV data, the results agree with the nondetections observed in the FUV band, as seen in Fig. 6.

Using the resulting z -PDF of hSDF0702.30a as a prior, the SNABC classifies this SN as a CC SN ($P(\text{Ia}) = 0.04$) at redshift $z = 1.95$, with $\chi^2 = 37$. The z -PDF of hSDF0702.30b, on the other hand, yields a different classification: ($P(\text{Ia}) = 0.51$) at redshift $z = 0.8$, with $\chi^2 = 0.4$. In this case, the SNABC chooses the smaller z -PDF peak at $z \approx 0.8$, instead of the main peak at $z \approx 1.7$, in order to avoid a high χ^2 value such as that achieved with the sharply peaked z -PDF of hSDF0702.30a. When run through

the SNABC with a flat z -PDF, the SN best resembles a CC SN at $z = 0.6$ with $\chi^2 = 0.2$. The z -PDF constructed from the best-fitting redshifts of the other SN host galaxies does not change this result much; the posterior redshift changes to $z = 0.7$, with a higher $\chi^2 = 0.5$.

In this case, the SNABC is dominated by the SN II-P LF. Since the colours of the SN match those of a SN II-P, it places it at $z < 1$, the redshift range where the apparent magnitude of the SN would still match the SN II-P LF. This is also the reason it produces a high χ^2 value when forced to higher redshifts. In summary, SNSDF0702.30 may be either a CC SN at $z = 0.6$ – 0.8 , or a non-Ia luminous SN at $z = 1.7$ – 1.95 . The possible observation of overluminous non-Ia SNe at high redshifts in our sample is discussed in Section 7.1.2, below. If it is a low- z CC SN, it will not be counted in the rates, as it is fainter than the detection limit adopted in Section 6. Since it may be a high- z non-Ia SN, we do not include this SN in our $1.5 < z < 2.0$ SN Ia sample.

5.1.4 SNSDF0705.17

SNSDF0705.17 was classified as a CC SN ($P(\text{Ia}) = 0$) at $z = 2.87$, with $\chi^2 = 61.6$. The offset of the candidate from its host galaxy is 0.15 ± 0.10 arcsec, or $\sim 1 \pm 1$ pixel. At $z = 2.87$, the object would have an intrinsic absolute magnitude of $M_{z'} = -21.27$ mag, making it too bright to be either

⁶ <http://users.obs.carnegiescience.edu/peng/work/galfit/galfit.html>

a SN Ia or a normal CC SN. This object appears in epoch 4, which is separated from epoch 3 by only ~ 90 days in the observer's frame. In the object's rest-frame, this interval corresponds to ~ 23 days. The high redshift, coupled with the high χ^2 value, raises the suspicion that this candidate, even though it shows no variability in other epochs, is still an AGN. Alternatively, the object might be a hyperluminous SN IIn, or even a pair-instability SN. Since both luminous SNe IIn and pair-instability SNe decay slowly (e.g., Di Carlo et al. 2002; Gal-Yam et al. 2009), if this object were one of the two it would likely have been detected in both epochs, unless it exploded between the two epochs. Our preferred conclusion is that this is an AGN and as such, we have removed it from our sample.

5.1.5 SNSDF0705.18

SNSDF0705.18 lies 3.06 ± 0.10 arcsec, about 3 half-light radii, from the closest (and only probable host) galaxy. We obtained a spectrum of this galaxy, which places it at $z = 1.41$. If this is indeed the SN's host galaxy, it is classified as a SN Ia, with $\chi^2 = 16.9$. The SNABC is sensitive to the z -PDF it receives as input, and since for this galaxy the input was a very narrow ($\sigma = 0.01$) Gaussian centred on the measured spec- z , we ran this SN through the SNABC once more, this time treating it as a hostless SN. This resulted in a classification as a CC SN ($P(\text{Ia}) = 0.29$) at a posterior redshift of 0.7, with a much better $\chi^2 = 0.5$. At this redshift, the SN would have an absolute magnitude of $M_z = -17.54$. The z' -band master image of epoch 4 has a limiting magnitude of 27.24 mag. At $z = 0.7$, a galaxy would have to be fainter than -15.9 mag so as not to be detected. This could mean that the candidate is indeed a CC SN that went off in a dwarf galaxy undetected in the SDF (see, e.g., Arcavi et al. 2010). Since the fit to a CC SN at $z = 0.7$ is much better than the earlier SN Ia classification, we treat this SN as a 'hostless,' intermediate redshift CC SN. As this SN is fainter than the detection limit adopted for this redshift bin (see Section 6, below), it will not be counted in the rates. To account for the possibility that this is a SN Ia in the range $1.0 < z < 1.5$, we add a systematic uncertainty of +1 to the number of SNe Ia in this bin.

5.1.6 SNSDF0705.30 and SNSDF0806.35

SNSDF0705.30 and SNSDF0806.35 are both classified as SNe Ia at high redshifts ($z = 1.93$ and $z = 1.94$, respectively), but with very high χ^2 values (33.8 and 22.1, respectively). While these SNe are both offset from the cores of their host galaxies (by 0.5 ± 0.1 and 0.7 ± 0.1 arcsec, respectively), they are much bluer than any of the Ia or CC SN spectral templates. SNSDF0806.35 has $R - i'$ and $i' - z'$ colours consistent with those of the $z = 1.189$ pulsational pair-instability SN SCP 06F6 (Barbary et al. 2009; Quimby et al. 2009), redshifted to $z = 1.94$. SNSDF0705.30, on the other hand, is even bluer. It might be a very blue non-Ia SN, or a background variable quasar. As both of these SNe are clearly not SNe Ia, we exclude them from our $1.5 < z < 2.0$ bin.

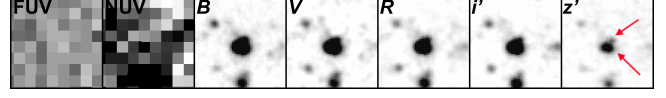


Figure 6. The possible host galaxies of SNSDF0702.30. The arrows in the z' -band image point to the two possible hosts: hSDF0702.30a is the resolved galaxy, while hSDF0702.30b is a compact source to the NW (above and to the right) of the latter. While there may be an ambiguous detection in the NUV band, both galaxies are clearly undetected in the FUV band. All tiles are 10 arcsec on a side.

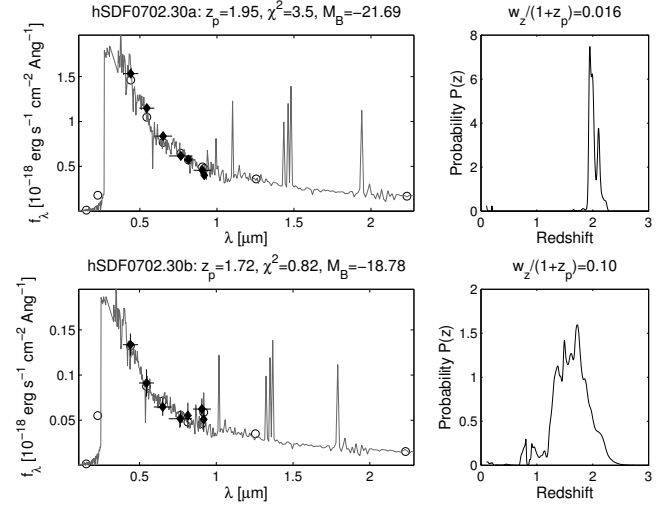


Figure 7. Photometric redshift derivation for the two possible hosts of SNSDF0702.30, shown in Fig. 6. The galaxy hSDF0702.30a appears on top, while hSDF0702.30b is below. Symbols as in Fig. 4. The first z -PDF is peaked at $z = 1.95$ with $w_z/(1+z) = 0.016$, and the second z -PDF is peaked at $z = 1.72$ with $w_z/(1+z) = 0.10$, where w_z is the width of the Gaussian, centred on z , which best fits the z -PDF.

6 DEBIASING: DERIVATION OF INTRINSIC SUPERNOVA TYPE AND REDSHIFT DISTRIBUTIONS

The success rate of the SNABC depends on the survey parameters (such as the number of observation bands and the survey depth). Thus, the raw distribution of SNe into SNe Ia and CC SNe may contain biases which need to be corrected before it can be used. We follow the debiasing procedure described in P07a and P07b. We use the spectral templates from N02 to simulate a sample of 40,000 SN light curves, divided into four subtypes: Ia, II-P, Ib/c, and IIn. These templates have been normalized so that the B -band absolute magnitude at maximum luminosity, for a stretch $s = 1$ (Perlmutter et al. 1999) SN Ia, is zero, in the Vega magnitude system. In order to construct the light curves in our sample, we follow the recipe outlined by Sullivan et al. (2006). For SNe Ia, the light curves are constructed according to:

$$m = m_{z=0,s=1} + M_B + \mu - \alpha(s - 1), \quad (4)$$

and

$$t_s = t_{s=1}\alpha, \quad (5)$$

where $m_{z=0,s=1}$ is the basic light curve, at $z = 0$ and with $s = 1$, constructed from the spectral templates; M_B is the peak brightness in the B band, drawn from a Gaussian centred on -19.37 mag, with a dispersion of $\sigma = 0.17$, mimicking the intrinsic SN Ia dispersion in peak brightness (Hamuy et al. 1995, 1996; Phillips et al. 1999); μ is the distance modulus; $\alpha = 1.52 \pm 0.14$ (Astier et al. 2006); s is the stretch parameter of the SN, which is modeled as a Gaussian centred on $s = 1$ with a dispersion of $\sigma = 0.25$, and allowed to vary in the range $0.7 \leq s \leq 1.3$, in line with Sullivan et al. (2006); and t_s is the age of the stretched-light-curve SN. The CC SN light curves are constructed in much the same way, but without any stretching. Host extinction is added using the extinction model from N06: the positive side of a Gaussian centred on $A_V = 0$, with a dispersion of $\sigma = 0.2$ for SNe Ia and $\sigma = 0.5$ for CC SNe, and truncated at $A_V = 1$.

As with our observed SN sample, one sixth of the simulated sample is assigned a random spec- z in the form of a Gaussian z -PDF with $\sigma = 0.01$. The rest of the SNe in the sample are randomly assigned a redshift from the z -PDF of the entire SDF, out to $z = 2$. Each simulated SN is assigned a ‘real’ redshift and a ‘measured’ redshift drawn from its z -PDF. This mimics the ZEBRA redshift determinations. While the simulated light curves are redshifted according to the real redshift, we keep the entire z -PDFs for the classification stage.

The resulting light curves are ‘observed’ at a random day, and each measurement is assigned an uncertainty according to the photometric uncertainties measured in our survey. At redshifts $z \leq 1$, the light curves do not cover the full time period during which SNe could have been detected by the depth of our survey. One way to overcome this problem would be to extrapolate the light curves, but this might introduce systematic errors that are difficult to quantify. Instead, we chose to impose a flux limit on the SNe found in these bins; by raising the detection limit we narrow the time period during which the SNe could have been observed, thus ensuring we stay within the bounds of the observed light curves.

In the $0.5 < z < 1.0$ bin, the detection limit was raised to 25.0 mag in the z' band for all epochs. This reduces the number of SNe in this bin from 86 to 29, of which 26 are classified as SNe Ia and 3 as CC SNe. In the $z < 0.5$ bin, the necessary flux limit leaves no SNe to work with; we thus cannot compute the SN rate in this bin. We note, however, that rates at $z < 1$ are much better measured by wider and shallower surveys that obtain light curves and spectroscopic confirmation for each SN (e.g. SDSS-II, SNLS). Our survey is designed specifically for detecting SNe at $z > 1$, and for classifying them with single-epoch photometry.

We measure the success fractions of the SNABC in each epoch of observations by selecting only those SNe that would have been detected by our survey (i.e., those SNe which are brighter in the z' band than 26.3, 26.6, 26.4, and 26.7 mag for epochs 2 through 5, respectively, in the $z > 1$ bins, and brighter than 25.0 mag in all epochs for the $0.5 < z < 1.0$ bin), leaving 3,500 SNe from each subtype. The surviving SNe are then classified by the SNABC, and their redshift is determined as in Section 5. Next, the SNe are distributed into three redshift bins ($0.5 < z < 1.0$, $1.0 < z < 1.5$, and $1.5 < z < 2.0$), and the success fraction in each bin is

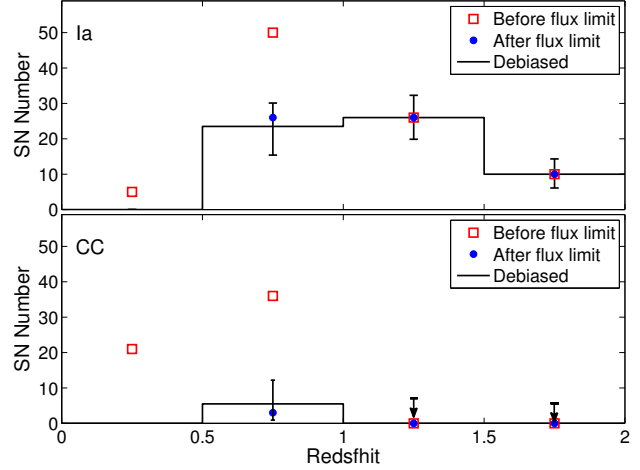


Figure 8. Observed (empty squares), flux-limited (filled circles), and debiased (solid line) SDF SN Ia and CC SN numbers. Filled squares denote the number of SNe in the $z < 1$ bins before application of the flux limit. SN Ia error bars are 1σ Poisson and classification uncertainties, added in quadrature. CC SN $0.5 < z < 1.0$ debiased error bar is 1σ Poisson and classification uncertainties, added in quadrature, and $z > 1$ debiased numbers are 2σ upper limits (arrows).

calculated by dividing the number of correctly classified SNe by the total number of SNe in that bin.

The resulting success fractions are used to calculate the probability of classifying a SN of any subtype as a SN Ia, as a function of the intrinsic distribution of SN subtypes (e.g., 10 per cent SN Ia, 40 per cent SN II-P, 20 per cent SN Ib/c, and 30 per cent SN IIn). Using steps of 2.5 per cent, there are 12,341 possible distributions. In each redshift bin, and for each possible distribution, the SN Ia success fraction is computed by summing the fraction of SNe Ia that were classified correctly, together with the fractions of CC SNe that were misclassified as SNe Ia. Each possible distribution is weighted according to the number of combinations in which the different CC SN subtypes may be distributed for a given fraction of SNe Ia (i.e., if the fraction of SNe Ia is 50 per cent, there are many different combinations of CC SN fractions, whereas if the SN Ia fraction is 100 per cent, there is only one possible combination).

After weighting the different distributions, we marginalize over all of the different combinations for a specific SN Ia fraction, and are left with the probability of classifying any SN as a SN Ia, as a function of the intrinsic SN subtype distribution. Using binomial statistics, this probability is used to answer the question: given the number of SNe classified by the SNABC as SNe Ia in a given redshift bin, the total number of SNe in that bin, and the probability of classifying any SN as a SN Ia, at a given intrinsic SN subtype distribution, what is the most probable fraction of SNe Ia in our sample? From the resulting PDF we select the most probable value as the true fraction of SNe Ia in each redshift bin, and define the 1σ uncertainty as the region that includes 68.3 per cent of the probability density. To this classification uncertainty we add, in quadrature, the statistical uncertainty, defined as the 1σ Poisson uncertainty of the debiased number of SNe Ia in

Table 3. SN Ia and CC SN numbers and rates

Subsample	$0.0 < z < 0.5$	$0.5 < z < 1.0$	$1.0 < z < 1.5$	$1.5 < z < 2.0$
Total	26	86	26	12
SNe Ia (raw)	5	50	26	10^a
SNe Ia (after flux limit)	0	26	26	10
SNe Ia (debiased) ^b	...	$23.5^{+5.4,+3.8}_{-5.3,-6.1}$	$26.0^{+6.2,+1.0}_{-5.1,-3.4}$	$10.0^{+4.3,+0.0}_{-3.1,-2.4}$
SN Ia rate ($10^{-4} \text{ yr}^{-1} \text{ Mpc}^{-3}$)	...	$0.77^{+0.22}_{-0.27}$	$0.67^{+0.16}_{-0.16}$	$0.64^{+0.27}_{-0.25}$
SN Ia rate without host-galaxy extinction	...	$0.70^{+0.15}_{-0.16}$	$0.57^{+0.14}_{-0.12}$	$0.50^{+0.24}_{-0.20}$
Effective redshift	...	0.74	1.23	1.69
CC SNe (raw)	21	36	0	0
CC SNe (after flux limit)	0	3	0	0
CC SNe (debiased) ^c	...	$5.5^{+2.9,+6.1}_{-2.3,-3.8}$	$< 3.8, +9.6$	$< 3.8, +5.7$
CC SN rate ($10^{-4} \text{ yr}^{-1} \text{ Mpc}^{-3}$)	...	$3.3^{+4.0}_{-2.7}$
CC SN rate without host-galaxy extinction	...	$1.4^{+1.7}_{-1.2}$
Effective redshift	...	0.66

^aTwo of the 12 SNe in this bin are clear non-Ia transients.

^bErrors are 1σ Poisson and classification uncertainties, respectively.

^cErrors in the $0.5 < z < 1.0$ bin are 1σ Poisson and classification uncertainties, respectively.

The $z > 1$ rates are upper limits. Errors are 2σ Poisson and classification uncertainties, respectively.

the redshift bin (or the Poisson uncertainty of the number of debiased CC SNe for the CC SN uncertainty).

The raw and debiased distributions of SNe Ia and CC SNe are presented in Fig. 8. The debiased number of SNe Ia is the same as the raw number in the two $z > 1$ bins, where our survey is insensitive to CC SNe, and thus free of contamination. In the $0.5 < z < 1.0$ bin, the number of SNe Ia falls to $23.5^{+5.4,+3.8}_{-5.3,-6.1}$, where the errors are 1σ Poisson and classification uncertainties, respectively. The post-debiasing number of CC SNe, on the other hand, rises to $5.5^{+2.9,+6.1}_{-2.7,-3.8}$.

7 SUPERNOVA RATES

In this section, we use the debiased distributions of SNe Ia and CC SNe to derive the SN Ia and CC SN rates in three redshifts bins: $0.5 < z < 1.0$, $1.0 < z < 1.5$, and $1.5 < z < 2.0$. Our rates are summarized in Table 3, and comparisons to the literature are given in Tables 4 and 5, and in Figures 9 and 10. All rates from the literature have been converted to $h = 0.7$. In cases where they are originally reported in SNUB (SNe per century per $10^{10} L_{\odot,B}$), we have converted them to volumetric rates using the redshift-dependent luminosity density function from B08:

$$j_B(z) = (1.03 + 1.76 \times z) \times 10^8 L_{\odot,B} \text{ Mpc}^{-3}. \quad (6)$$

7.1 The type Ia supernova rate

The volumetric SN Ia rate is

$$R_{\text{Ia}}(\langle z \rangle_i) = \frac{N_{\text{Ia},i}}{\int t_v(z) \frac{dV}{dz} dz}, \quad (7)$$

where $\langle z \rangle_i$ is the effective redshift of each redshift bin i , $N_{\text{Ia},i}$ is the number of debiased SNe Ia in bin i , and $t_v(z)$ is the survey visibility time, integrated over the comoving survey volume element dV , at all redshifts z within bin i .

The visibility time is the total amount of time we could

have observed a SN, given the parameters of our survey. At a given redshift, we need to consider the dispersion in light curves that originates in three separate effects: the intrinsic dispersion in peak magnitude, the stretch-luminosity relation, and the host-galaxy extinction. To account for these different effects, we calculate the visibility time of each possible light curve, weight it by its probability (which is just the product of the probabilities of the separate effects), and sum over all possible combinations.

As in the previous section, we construct each possible light curve according to Equation 4. We construct light curves with all the possible combinations of peak magnitude, stretch, and extinction, where M_B is allowed to vary as a Gaussian in the 2σ range around -19.37 mag (where $1\sigma = 0.17$); the stretch parameter s is allowed to vary as a Gaussian centred on $s = 1$ with a dispersion of 0.25 in the range $0.7 \leq s \leq 1.3$, with $\alpha = 1.52$; and A_V ranges between 0 and 1 mag according to the N06 model.

Each point in the light curve is multiplied by the appropriate detection efficiency taken from the functions in Section 3.2, and the entire light curve is then summed over the time it lies above the detection efficiency limit (the 50 per cent detection efficiency limits for the $z > 1$ bins, and 25.0 mag in the $0.5 < z < 1.0$ bin). Finally, we sum over the different epochs (since for each epoch the detection efficiency limit is different), and end up with the visibility time of our entire survey. Symbolically,

$$t_v(z) = \sum_{\text{epoch}} \iiint dM_B ds dA_V p(M_B) p(s) p(A_V) \times \int_{m > m_{1/2}} \epsilon[m_z(t)] dt. \quad (8)$$

We take the weighted average of the redshifts in a bin as the bin's effective redshift, where the weight is the visibility time integrated over the volume element within that bin:

$$\langle z \rangle_i = \frac{\int t_v z dV}{\int t_v dV}. \quad (9)$$

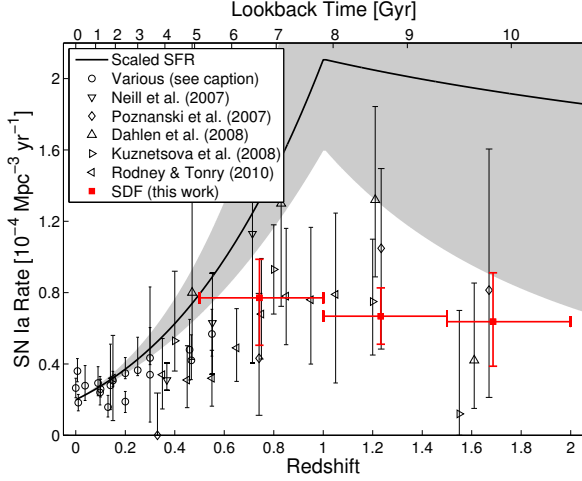


Figure 9. SN Ia rates from the SDF (filled squares) compared to rates from the literature. Circles denote low- z data from Cappellaro et al. (1999), Hardin et al. (2000), Pain et al. (2002), Madgwick et al. (2003), Tonry et al. (2003), Blanc et al. (2004), Neill et al. (2006), Botticella et al. (2008), Dilday et al. (2008), Horesh et al. (2008), Dilday et al. (2010a), and Li et al. (2010a). Down-turned triangles are for Neill et al. (2007). The corrected IfA Deep Survey rates from Rodney & Tonry (2010) are left-facing triangles. The GOODS rates from Dahlen et al. (2008) are denoted by upturned triangles. Right-facing triangles are for Kuznetsova et al. (2008). Our initial SDF results (Poznanski et al. 2007b) are shown as diamonds. The cosmic SFH from Y08, has been scaled to fit the low- z data. The shaded area denotes the plausible range of SFHs with power-law slopes between 3 and 4, out to $z = 1$, and between -2 and 0 for $z > 1$. All vertical error bars include statistical and systematic uncertainties added in quadrature. Horizontal error bars indicate the SDF redshift bins.

The uncertainties of the rates are the classification and Poisson uncertainties of the debiased SN Ia numbers, propagated and added in quadrature. To test how the uncertainties in the detection efficiency functions, as plotted in Figure 2, affect the rates, we ran 500 Monte Carlo simulations in which each efficiency measurement was varied according to its uncertainty. This produced variations in the detection efficiency limits of ± 0.1 mag. This propagates to a 1σ dispersion in the SN Ia rates that is between one and two orders of magnitude smaller than our main uncertainties, thus having a negligible effect on the resulting rates.

If host-galaxy extinction is not taken into account, the resulting SN Ia rates (in units of 10^{-4} SNe $\text{yr}^{-1} \text{Mpc}^{-3}$) are $R_{\text{Ia}}(\langle z \rangle = 0.74) = 0.70^{+0.15}_{-0.16}$, $R_{\text{Ia}}(\langle z \rangle = 1.23) = 0.57^{+0.14}_{-0.12}$, and $R_{\text{Ia}}(\langle z \rangle = 1.69) = 0.50^{+0.24}_{-0.20}$. Once both host-galaxy extinction and the stretch-luminosity relation have been taken into account, the resulting SN Ia rates (in the same units) are $R_{\text{Ia}}(\langle z \rangle = 0.74) = 0.75^{+0.21}_{-0.26}$, $R_{\text{Ia}}(\langle z \rangle = 1.23) = 0.62^{+0.15}_{-0.15}$, and $R_{\text{Ia}}(\langle z \rangle = 1.69) = 0.58^{+0.25}_{-0.23}$.

7.1.1 High-redshift dust

As star formation increases with redshift, so does injection of dust into the interstellar medium, leading to an expected increase of extinction with redshift (e.g., Holwerda 2008). This effect should lead to a decrease in the number of observed SNe at high redshifts, until the SFH peaks at

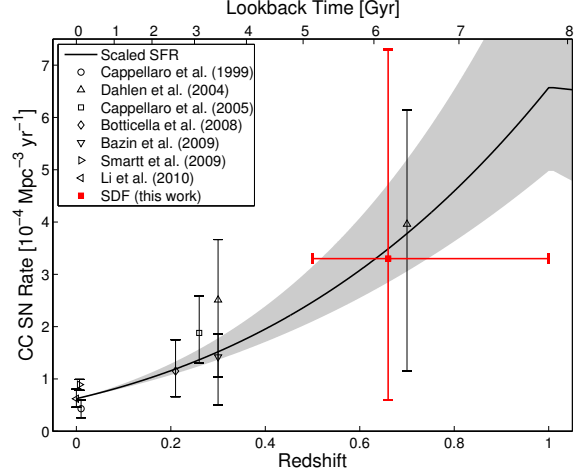


Figure 10. CC SN rate from the SDF (filled square) compared to rates from the literature: Cappellaro et al. 1999 (circle), Dahlen et al. 2004 (upward triangles), Cappellaro et al. 2005 (square), Botticella et al. 2008 (diamond), and Bazin et al. 2009 (downward triangle). As in Fig. 9, the SFH from Y08 has been scaled to fit the low- z data. All vertical error bars from the literature are 1σ uncertainties. The horizontal error bar indicates the SDF redshift bin.

$z = 1-2.5$. Throughout this work we have neglected this effect, assuming the amount of host-galaxy extinction remains constant with redshift. In a similar vein, Mannucci, Della Valle, & Panagia (2007) have shown that at high redshifts ($z > 1$) a large fraction of SNe, both CC SNe and SNe Ia, would be missed in optical surveys, due to extinction by dust in massive starburst galaxies, which make up a larger fraction of the galaxy population at higher redshifts (Le Floch et al. 2005; Daddi et al. 2005; Pérez-González et al. 2005). Using the Mannucci, Della Valle, & Panagia (2006) DTD model, Mannucci et al. (2007) calculated that in the range $1.0 < z < 2.0$, 15 to 35 per cent of SNe Ia would be missed. Assuming a power-law DTD model with a slope of -1 , the fraction of missing SNe Ia would be 5–13 per cent in the above redshift range (F. Mannucci, private communication). Correcting the SN Ia rates for this effect raises their values (in the same units) to $R_{\text{Ia}}(\langle z \rangle = 0.74) = 0.77^{+0.22}_{-0.27}$, $R_{\text{Ia}}(\langle z \rangle = 1.23) = 0.67^{+0.16}_{-0.16}$, and $R_{\text{Ia}}(\langle z \rangle = 1.69) = 0.64^{+0.27}_{-0.25}$.

7.1.2 Contamination from high- z non-Ia transients

While our survey is largely insensitive to CC SNe at $z > 1$, there remains the possibility of contamination by non-Ia luminous SNe (e.g., Smith et al. 2007; Quimby et al. 2007; Barbary et al. 2009). As detailed in Section 5.1, we have discovered two luminous non-Ia SNe in the $1.5 < z < 2.0$ bin. This ratio of 2:10 non-Ia SNe to SNe Ia is consistent with the 1:11 ratio found by Barbary et al. (2010), who found one non-Ia transient (SCP 06F6) and 11 field SNe Ia in the redshift range $z = 0.6-1.3$.

As for contamination by AGNs, the extremely blue colours of SNSDF0705.30 and the classification of SNSDF0705.17 as a CC SN at $z = 2.87$ hint that these objects might be variable background quasars, as detailed

Table 4. SN Ia rate measurements

Redshift	N_{Ia}	Rate [$10^{-4} \text{ yr}^{-1} \text{ Mpc}^{-3}$]	Reference
$< 0.0066^a$	37	$0.36^{+0.07}_{-0.06}$	Smartt et al. (2009)
0.01	70	0.183 ± 0.046	Cappellaro et al. (1999) ^b
$< 0.019^a$	274	$0.265^{+0.034+0.043}_{-0.033-0.043}$	Li et al. (2010a)
0.0375	516 ^c	$0.278^{+0.112+0.015}_{-0.083-0.000}$	Dilday et al. (2010a)
0.09	17	$0.29^{+0.09}_{-0.07}$	Dilday et al. (2008)
0.098	19	$0.24^{+0.12}_{-0.12}$	Madgwick et al. (2003) ^b
0.1	516 ^c	$0.259^{+0.052+0.018}_{-0.044-0.001}$	Dilday et al. (2010a)
0.13	14	$0.158^{+0.056+0.035}_{-0.043-0.035}$	Blanc et al. (2004) ^b
0.14	4	$0.28^{+0.22+0.07}_{-0.13-0.04}$	Hardin et al. (2000) ^b
0.15	516 ^c	$0.307^{+0.038+0.035}_{-0.034-0.005}$	Dilday et al. (2010a)
0.15	1.95	$0.32^{+0.23+0.07}_{-0.23-0.06}$	Rodney & Tonry (2010)
0.2	17	$0.189^{+0.042+0.018}_{-0.034-0.015} \pm 0.42$	Horesh et al. (2008)
0.2	516 ^c	$0.348^{+0.032+0.082}_{-0.030-0.007}$	Dilday et al. (2010a)
0.25	1	0.17 ± 0.17	Barris & Tonry (2006)
0.25	516 ^c	$0.365^{+0.031+0.182}_{-0.028-0.012}$	Dilday et al. (2010a)
0.3	31.05 ^d	$0.34^{+0.16+0.21}_{-0.15-0.22}$	Botticella et al. (2008)
0.3	516 ^c	$0.434^{+0.037+0.396}_{-0.034-0.016}$	Dilday et al. (2010a)
0.35	5	0.530 ± 0.024	Barris & Tonry (2006)
0.35	4.01	$0.34^{+0.19+0.07}_{-0.19-0.03}$	Rodney & Tonry (2010)
0.368	17	$0.31^{+0.05+0.08}_{-0.05-0.03}$	Neill et al. (2007)
0.40	5.44	$0.53^{+0.39}_{-0.17}$	Kuznetsova et al. (2008)
0.45	9	0.73 ± 0.24	Barris & Tonry (2006)
0.45	5.11	$0.31^{+0.15+0.12}_{-0.15-0.04}$	Rodney & Tonry (2010)
0.46	8	0.48 ± 0.17	Tonry et al. (2003)
0.467	73	$0.42^{+0.06+0.13}_{-0.06-0.09}$	Neill et al. (2006)
0.47	8	$0.80^{+0.37+1.66}_{-0.27-0.26}$	Dahlen et al. (2008)
0.55	38	$0.568^{+0.098+0.098}_{-0.088-0.088}$	Pain et al. (2002) ^a
0.55	29	2.04 ± 0.38	Barris & Tonry (2006)
0.55	6.49	$0.32^{+0.14+0.07}_{-0.14-0.07}$	Rodney & Tonry (2010)
0.552	41	$0.63^{+0.10+0.26}_{-0.10-0.27}$	Neill et al. (2007)
0.65	23	1.49 ± 0.31	Barris & Tonry (2006)
0.65	10.09	$0.49^{+0.17+0.14}_{-0.17-0.08}$	Rodney & Tonry (2010)
0.714	42	$1.13^{+0.19+0.54}_{-0.19-0.70}$	Neill et al. (2007)
0.74	5.5	$0.43^{+0.36}_{-0.32}$	Poznanski et al. (2007b)
0.74	23.5	$0.77^{+0.22}_{-0.27}$	SDF (this work)
0.75	28	1.78 ± 0.34	Barris & Tonry (2006)
0.75	14.29	$0.68^{+0.21+0.23}_{-0.21-0.14}$	Rodney & Tonry (2010)
0.80	18.33	$0.93^{+0.25}_{-0.25}$	Kuznetsova et al. (2008)
0.83	25	$1.30^{+0.33+0.73}_{-0.27-0.51}$	Dahlen et al. (2008)
0.85	15.43	$0.78^{+0.22+0.31}_{-0.22-0.16}$	Rodney & Tonry (2010)
0.95	13.21	$0.76^{+0.25+0.32}_{-0.25-0.26}$	Rodney & Tonry (2010)
1.05	11.01	$0.79^{+0.28+0.36}_{-0.28-0.41}$	Rodney & Tonry (2010)
1.20	8.87	$0.75^{+0.35}_{-0.30}$	Kuznetsova et al. (2008)
1.21	20	$1.32^{+0.36+0.38}_{-0.29-0.32}$	Dahlen et al. (2008)
1.23	10.0	$1.05^{+0.45}_{-0.56}$	Poznanski et al. (2007b)
1.23	26.0	$0.67^{+0.16}_{-0.16}$	SDF (this work)
1.55	0.35	$0.12^{+0.58}_{-0.12}$	Kuznetsova et al. (2008)
1.61	3	$0.42^{+0.39+0.19}_{-0.23-0.14}$	Dahlen et al. (2008)
1.67	3.0	$0.81^{+0.79}_{-0.60}$	Poznanski et al. (2007b)
1.69	10.0	$0.64^{+0.27}_{-0.25}$	SDF (this work)

Note – Redshifts are means over the redshift intervals probed by each survey. N_{Ia} is the number of SNe Ia used to derive the rate. Where necessary, rates have been converted to $h = 0.7$.

^aSmartt et al. (2009) and Li et al. (2010a) consider SNe Ia within 28 and 80 Mpc, respectively.

^bRates have been converted to volumetric rates using Equation 6.

^cDilday et al. (2010a) compute their rates using 516 SNe Ia in the redshift range $z < 0.5$.

^dBotticella et al. (2008) found a total of 86 SN candidates of all types. See their section 5.2 for details on their various subsamples and classification techniques.

Table 5. CC SN rate measurements

Redshift	N_{CC}	Rate [$10^{-4} \text{ yr}^{-1} \text{ Mpc}^{-3}$]	Reference
$< 0.0066^a$	92	$0.89^{+0.07+0.11}_{-0.07-0.09}$	Smartt et al. (2009)
0.01	67	0.43 ± 0.17	Cappellaro et al. (1999) ^b
$< 0.014^a$	440	$0.62^{+0.07+0.17}_{-0.07-0.15}$	Li et al. (2010a)
0.21	44.95 ^c	$1.15^{+0.43+0.42}_{-0.33-0.36}$	Botticella et al. (2008)
0.26	31.2	$1.88^{+0.71}_{-0.58}$	Cappellaro et al. (2005) ^b
0.3	17	$2.51^{+0.88+0.75}_{-0.75-1.86}$	Dahlen et al. (2004)
0.3	117	$1.63^{+0.34+0.37}_{-0.34-0.28}$	Bazin et al. (2009)
0.66	5.5	$3.3^{+4.0}_{-2.7}$	SDF (this work)
0.7	17	$3.96^{+1.03+1.92}_{-1.06-2.60}$	Dahlen et al. (2004)

^aSmartt et al. (2009) and Li et al. (2010a) consider CC SNe within 28 and 60 Mpc, respectively.

Note – ^{b,c}Same as in Table 4.

in Section 5.1. This is consistent with the expected number of contaminating AGNs in our sample, as detailed in Section 4.1. In summary, beyond the non-Ia objects we have identified, contamination of the $1.5 < z < 2.0$ SN Ia sample is unlikely.

7.1.3 Probing the UV part of the SN spectrum

From a theoretical standpoint, the spectra of SNe Ia at high redshifts may differ from their low-redshift counterparts due to changes in, for example, progenitor metallicity. Such differences are expected to show up in the UV part of the SN Ia spectrum, introducing a possible systematic uncertainty into any survey (such as the current work) which probes this part of the spectrum (Hoefflich, Wheeler, & Thielemann 1998; Lentz et al. 2000; Sauer et al. 2008). Several recent surveys have found evidence for such differences between low- and high-redshift SNe Ia (e.g., Kessler et al. 2009; Cooke et al. 2010; Foley et al. 2010), which might provide an additional explanation for the high χ^2 values of the two peculiar SNe in our $1.5 < z < 2.0$ sample. On the other hand, it is possible that the perceived differences are due to problems in observing the rest-frame UV at low redshift from the ground, as a result of PSF broadening and atmospheric extinction, or poor calibrators (Jha et al. 2006).

7.2 The core-collapse supernova rate

Since our survey is insensitive to normal CC SNe at redshifts higher than 1, we do not use the debiased results to derive the rates in the $1.0 < z < 1.5$ and $1.5 < z < 2.0$ redshift bins. We now proceed to derive the CC SN rate in the $0.5 < z < 1.0$ redshift bin.

To account for the division of CC SNe into subtypes, in the calculation of the visibility time we have weighted the contribution of each subtype according to its fraction of the total CC SN population, and then summed the different contributions. The CC SN subtype fractions were taken from the volume-limited sample of Li et al. (2010b), with two alterations: (a) the SN II-P and SN II-L fractions have been combined, as the separation between these subclasses is currently ill-defined (Poznanski et al., in preparation); and (b) the SN Ib/c and SN IIb fractions have also been combined, since their light curves are nearly identical (Benson et al.

1994). The final volume-limited CC SN fractions are 60.0 per cent II-P/L, 33.5 per cent Ib/c/IIb, and 6.5 per cent IIn. We note that Li et al. (2010b,a) only targeted $\sim L_*$ galaxies, and so the CC SN fractions and rates might be different for an untargeted survey (e.g., Arcavi et al. 2010). We calculate the flux-limited fractions at the effective redshift of $z = 0.66$ as being 37 per cent II-P/L, 44 per cent Ib/c/IIb, and 19 per cent IIn.

As in the previous section, the visibility time of each CC SN subtype was derived using Equation 8, but without stretch. In the present case, M_B was limited to the 2σ range around the peak magnitude of each subtype. The probability for A_V was drawn from a one-sided Gaussian PDF centred on 0 with a dispersion of $\sigma = 0.5$, and the probability for M_B was drawn from the LF of each subtype. Without host-galaxy extinction, the rates of each CC SN subtype (in units of $10^{-4} \text{ SNe yr}^{-1} \text{ Mpc}^{-3}$) are 1.1 for SNe II-P/L, 0.2 for SNe Ib/c/IIb, and 0.1 for SNe IIn. This results in an overall rate of $R_{\text{CC}}(\langle z \rangle = 0.66) = 1.4^{+1.7}_{-1.2} \times 10^{-4} \text{ SNe yr}^{-1} \text{ Mpc}^{-3}$. Once host-galaxy extinction is added, the rates of each CC SN subtype (in the same units) become: 2.0 for SNe II-P/L, 0.4 for SNe Ib/c/IIb, and 0.1 for SNe IIn. This yields an overall rate of $R_{\text{CC}}(\langle z \rangle = 0.66) = 2.5^{+3.0}_{-2.0} \times 10^{-4} \text{ SNe yr}^{-1} \text{ Mpc}^{-3}$. After correcting for the fraction of CC SNe missed due to high-redshift dust (Mannucci et al. 2007), the final CC SN rate is $R_{\text{CC}}(\langle z \rangle = 0.66) = 3.3^{+4.0}_{-2.7} \times 10^{-4} \text{ SNe yr}^{-1} \text{ Mpc}^{-3}$. This value is consistent with both the rate derived by D04 in this redshift bin and with the scaled Y08 SFH at that redshift, as shown in Fig. 10. We present a summary of CC SN rates from the literature, along with our measured rate at $\langle z \rangle = 0.66$, in Table 5.

8 THE TYPE IA SUPERNOVA DELAY-TIME DISTRIBUTION

In this Section we make use of our measured SN Ia rates, together with published rates at various redshifts, to recover the DTD. The different SN Ia rates used in our fits are presented in Table 4. Where necessary (Cappellaro et al. 1999; Hardin et al. 2000; Pain et al. 2002; Madgwick et al. 2003; Blanc et al. 2004), rates from the literature have been converted to volumetric rates using the redshift-dependent luminosity density function from B08 (see Equation 6). Furthermore, all rates have been converted to $h = 0.7$. We make

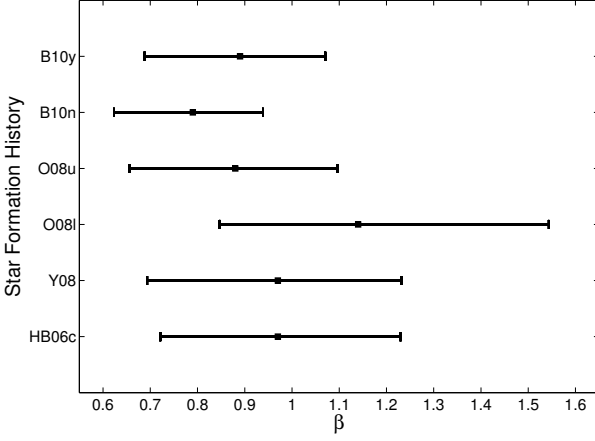


Figure 11. Best-fitting values and 68 per cent statistical uncertainties of the slope β of a power-law DTD of the form $\Psi(t) = \Psi_1(t/1 \text{ Gyr})^\beta$, when convolved with various SFHs, as marked. See Table 6 for SFH abbreviations and parameters.

use of all the SN Ia rate measurements in Table 4, except for the Barris & Tonry (2006) measurements, which have been superseded by Rodney & Tonry (2010); the Kuznetsova et al. (2008) measurements, which make use of much the same data as D08; and our initial results reported by P07b, which are superseded by the present results. In total, there are 37 SN Ia rate measurements, of which 32 are at $z < 1$ and 5 at $z > 1$.

We recover the DTD by convolving different trial DTDs with various SFH fits from the literature, resulting in a model SN Ia rate evolution. One such SFH is the one presented in fig. 2 of HB06 (HB06c). Other recent estimates of the SFH and their parametrizations (e.g., Y08, O08, and B10) can be approximated by broken power laws, with a break at z between 1–2.5, and various power-law indices above and below the break. To test the systematic uncertainty in our DTD derivation produced by this range of possible SFHs, we parametrize the SFH as being proportional to $(1+z)^\gamma$, with γ in the range 3–4 at $z < 1$, a break at $z = 1$, and γ values in the range -2 –0 at $z > 1$. We also test the models that appear in fig. 16 of B10, as their shallower power law and later break at $z = 2.5$ will have an additional systematic effect on the slope of the DTD. This range of parametrizations covers most of the SFHs that have been recently proposed. The indices, breaks, and normalizations of each SFH at $z = 0$ are collected in Table 6. For a given SFH, variations of the normalization will translate to inverse scalings of the amplitude of the best-fitting DTD, without affecting the DTD shape, which is our main interest here. There remains considerable debate among different authors as to the amount and the redshift dependence of extinction corrections in SFH estimates (see, e.g., B10; Robertson et al. 2010). Different extinction correction choices can shift much or all of a SFH curve up or down by factors of up to 7 or so. To account for this uncertainty, we also calculate the range in DTD amplitude, Ψ_1 , that results when the SFH varies between the extreme case of no extinction (B10) and the HB06c level.

Throughout this derivation we assume a ‘diet-Salpeter’

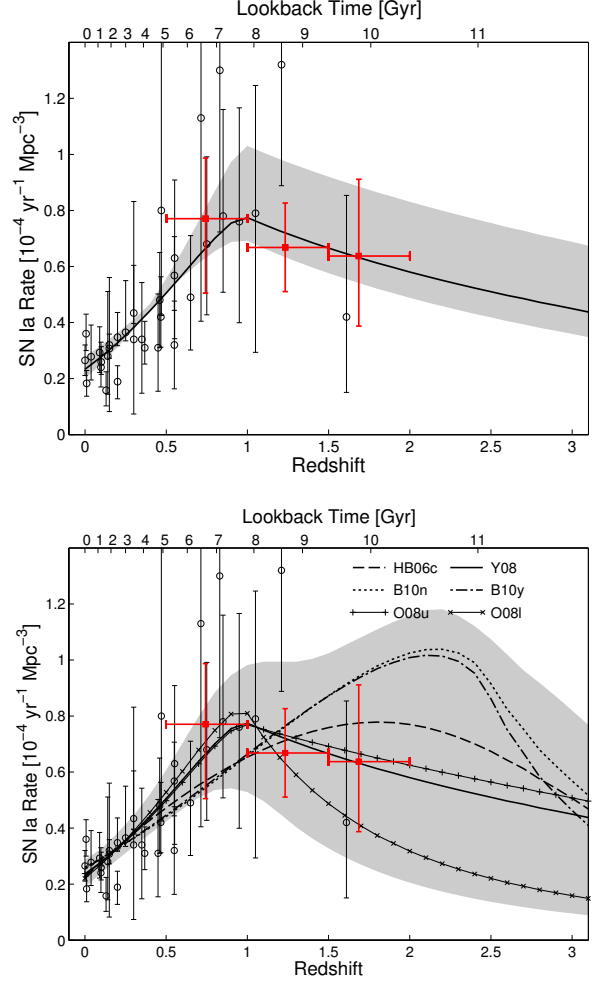


Figure 12. Top panel: Observed SN Ia rates compared to prediction from convolution of the Y08 SFH with a best-fitting power-law DTD of the form $\Psi(t) = \Psi_1(t/1 \text{ Gyr})^\beta$ (solid line). Non-independent measurements, which are therefore excluded from the fits, are not plotted – Kuznetsova et al. (2008) and P07b, which are superseded by D08 and this work, respectively. The shaded area is the confidence region resulting from the 68 per cent statistical uncertainty of β from the convolution of the DTD with the Y08 SFH fit. Bottom panel: Same as top panel, but for each of the SFHs in Table 6, and showing the combined effect of the 68 per cent statistical uncertainties of β .

initial mass function (IMF; Bell et al. 2003). This IMF assumption means that the SFHs of HB06, Y08, and B10, which assumed a Salpeter (1955) IMF, are scaled down by a factor of 0.7. We then use the minimal χ^2 statistic to find the best-fitting values of the parameters of the DTD, along with their statistical 68 and 95 per cent confidence regions, which are defined as the values at which χ^2 reaches the critical values corresponding to probabilities of 68 or 95 per cent. To the statistical uncertainty of the parameters we add the systematic uncertainty which originates in the shapes of the different SFHs. Finally, for each model we calculate the number of SNe Ia per formed stellar mass, integrated over a Hubble time.

We first test a power-law DTD of the form $\Psi(t) = \Psi_1(t/1 \text{ Gyr})^\beta$. Such a power law, with $\beta \approx -1$, is generic to

the DD scenario, where two WDs merge due to loss of energy and angular momentum to gravitational waves (see, e.g., Maoz et al. 2010b). Several recent experiments, in different environments and different redshifts, have indeed found best-fitting DTDs consistent with this form (Totani et al. 2008; Maoz & Badenes 2010; Maoz et al. 2010a,b). The DTD is set to zero for the first 40 Myr, until the formation of the first WDs. We fit for the normalization Ψ_1 and the slope β . Based on the Y08 SFH fit, we find best-fitting values of $\beta = 0.97^{+0.26(0.40)}_{-0.28(0.43)}$, where the statistical uncertainties are the 68 and 95 (in parentheses) per cent confidence regions, respectively. The range of SFHs tested here adds a systematic uncertainty of $^{+0.17}_{-0.18}$. The best-fitting values of β for all six SFHs, with their respective reduced χ^2 values, appear in Table 6. These best-fitting values result in reduced χ^2 values of 0.81 to 1.00, for 35 degrees of freedom (DOF) for all SFH fits. The number of SNe Ia per formed stellar mass, integrated over a Hubble time, lies in the range $N_{\text{SN}}/M_* = (0.74\text{--}5.4) \times 10^{-3} \text{ M}_\odot^{-1}$. The best-fitting values of β are presented in Fig. 11, and the resulting SN Ia rate evolution tracks are presented in Fig. 12.

Whereas the power law discussed above extends all the way back to $t = 40$ Myr, it is possible that at early times the DTD is dictated not by the WD merger rate, but rather by the supply of progenitor systems. Pritchett, Howell, & Sullivan (2008) have suggested a $t^{-1/2}$ power-law DTD, which is proportional to the formation rate of WDs. A pure $t^{-1/2}$ power law, convolved with the HB06c, Y08, and O08l SFHs, produces fits with a minimal $\chi^2 > 1.42$ for 36 DOF, ruling out this model at the 95 per cent confidence level. The B10n, B10y, and O08u SFHs result in fits with minimal χ^2 values of 0.80, 1.40, and 1.36 (respectively), which are marginally acceptable. Matteucci et al. (2009) also argue against this model, as it does not reproduce the observed G-dwarf metallicity distribution in the solar vicinity (see their fig. 7). The resulting SN Ia rate evolution tracks are presented in the top panel of Fig. 13.

Another possibility is that the DTD is controlled by the WD formation rate up to some characteristic time t_c , beyond which the combined mass of the merged WDs is insufficient to produce a SN Ia event; at this point the formation rate of lighter WDs no longer affects the production of SNe Ia, and the merger rate sets the DTD. The Greggio (2005) DD3-close model, for example, is such a broken power law, with $t^{-1/2}$, $t^{-1.3}$, and a break at $t_c = 0.4$ Gyr. This value for t_c corresponds to the lifetime of 3M_\odot stars. A larger value of t_c would imply that WD binaries with a smaller primary mass can explode as SNe Ia, and ultimately contribute to the observed SN Ia rate. We therefore investigate whether the SN Ia rate data may be fit by a broken power law behaving as $t^{-1/2}$ at $t < t_c$, and as t^{-1} thereafter. Fitting for t_c and the normalization Ψ_1 , we find that t_c lies in the 68 per cent confidence range 0.04–5.4 Gyr. As a $t^{-1/2}$ power-law DTD at all times is still an acceptable option, owing to the systematic uncertainty in the SFH, we cannot constrain t_c at the 95 per cent confidence level. The best-fitting parameters result in reduced χ^2 values of 0.82–0.92, for 35 DOF for all SFH fits. The integrated number of SNe Ia per stellar mass formed resulting from this DTD lies in the range $N_{\text{SN}}/M_* = (0.62\text{--}5.3) \times 10^{-3} \text{ M}_\odot^{-1}$, where the uncertainty again derives from the normalizations of the SFHs. This range is consistent with the result obtained with the

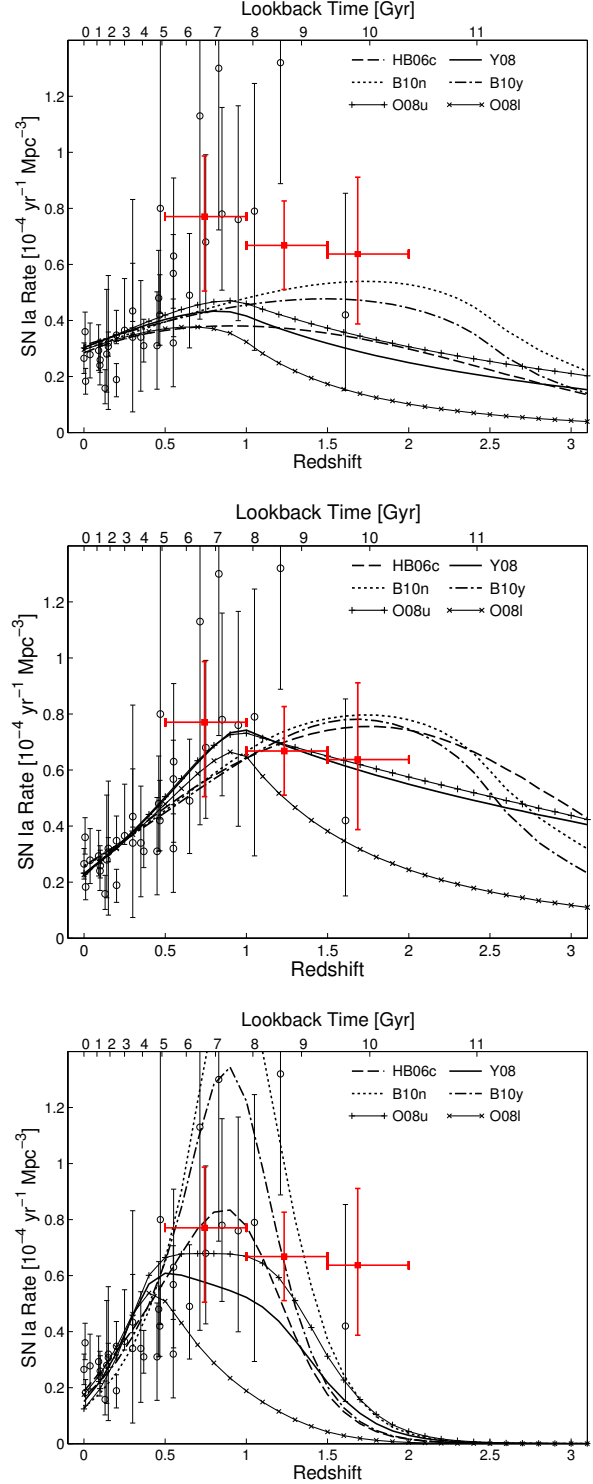


Figure 13. Observed SN Ia rates compared to predictions from convolution of the SFHs in Table 6 with a best-fitting (top) power-law DTD of the form $\Psi(t) = \Psi_1(t/1 \text{ Gyr})^{-1/2}$; (centre) broken power-law DTD of the form $\Psi(t) \propto t^{-1/2}$ up to t_c , and $\Psi(t) \propto t^{-1}$ afterwards; and (bottom) D08 Gaussian DTD. Symbols as marked.

Table 6. Star formation histories and resultant best-fitting DTD parameters.

SFH		Power-law DTD		Broken power-law DTD ^a	
Ref. ^b	Parametrization ^c	β^d	χ^2/DOF	t_c [Gyr] ^e	χ^2/DOF
HB06c	Cole et al. (2001) with values from HB06	$0.97^{+0.26(0.44)}_{-0.25(0.42)}$	0.88	$0.1^{+2.8}_{-0.1}$	0.88
Y08	$S(0) = 17.8$, $\gamma_1 = 3.4$, $z_b = 1$, $\gamma_2 = -0.3$	$0.97^{+0.26(0.40)}_{-0.28(0.43)}$	0.81	$0.17^{+2.83}_{-0.13}$	0.82
O08l	$S(0) = 17.8$, $\gamma_1 = 3$, $z_b = 1$, $\gamma_2 = -2$	$1.1^{+0.4(0.7)}_{-0.3(0.5)}$	0.87	$0.05^{+0.60}_{-0.01}$	0.91
O08u	$S(0) = 17.8$, $\gamma_1 = 4$, $z_b = 1$, $\gamma_2 = 0$	$0.9 \pm 0.2(0.3)$	0.81	$0.7^{+3.0}_{-0.7}$	0.82
B10n	$S(0) = 1.6$, $\gamma_1 = 3$, $z_b = 2.5$, $\gamma_2 = -2.8$	$0.79^{+0.15(0.27)}_{-0.17(0.26)}$	1.00	$2.5^{+4.1}_{-2.2}$	0.90
B10y	$S(0) = 10.0$, $\gamma_1 = 2.5$, $z_b = 2.5$, $\gamma_2 = -4$	$0.89^{+0.18(0.34)}_{-0.20(0.39)}$	0.96	$1.4^{+3.1}_{-1.4}$	0.92

^a $\Psi(t) \propto t^{-1/2}$ power law at $t < t_c$, and $\Psi(t) \propto t^{-1}$ at $t > t_c$.

^bSFH references: HB06c – Hopkins & Beacom (2006); Y08 – Yüksel et al. (2008); O08l and O08u – Oda et al. (2008); B10y and B10n – Bouwens et al. (2010), with and without extinction correction, respectively.

^cExcept for HB06c, all other SFHs are parametrized as broken power laws of the form $S(z) = S(0)(1+z)^{\gamma_i}$, with γ_1 at $z < z_b$, and γ_2 at $z > z_b$. $S(0)$ is in units of $10^{-3} \text{ M}_\odot \text{ yr}^{-1} \text{ Mpc}^{-3}$.

^dThe first and second errors (in parentheses) are 68 and 95 per cent confidence regions, respectively, for the slope β of the power-law DTD.

^eErrors are 68 per cent confidence regions for t_c , the break between a $t^{-1/2}$ and a t^{-1} power law.

single power-law DTD. The best-fitting parameters, along with reduced χ^2 values, are presented in Table 6, and the resulting SN Ia rate evolution tracks are presented in the centre panel of Fig. 13.

Finally, D04, D08, and Strolger et al. (2004, 2010) advocate a Gaussian DTD with parameters $\tau = 3.4$ Gyr and $\sigma = 0.2\tau$. D04 used the SFH determined by Giavalisco et al. (2004) in order to derive the parameters of the Gaussian DTD. As we use different SFHs, we leave the normalization Ψ_G as a free parameter. The best-fitting value, derived with the HB06c SFH fit, has a minimal $\chi^2 = 1.25$ for 36 DOF, which is higher than the 68 per cent χ^2 confidence region. All the other SFHs result in best-fitting values with minimal $\chi^2 > 1.63$, ruling out this model at the 99 per cent confidence level. The resulting SN Ia rate evolution tracks are plotted in the bottom panel of Fig. 13.

9 THE TYPE IA SUPERNOVA RATE AT REDSHIFT > 2 AND COSMIC IRON ACCUMULATION

Our analysis, above, has provided the most precise determination to date of the SN Ia rate at $1 < z < 2$. As seen in the bottom panel of Fig. 12, the best-fitting power-law DTD, convolved with each SFH, can also be used to predict the SN Ia rate at $z > 2$. The shaded regions in the figure show the uncertainty regions produced by the statistical and systematic uncertainties of the DTD slope β , where the statistical uncertainties result from the SN Ia rate measurements, and the systematic uncertainties result from the uncertainty in the slope of the SFHs at $z < z_b$.

Following Blanc & Greggio (2008), we can use our results to calculate the mean cosmic accumulation of iron. A typical SN Ia produces $\sim 0.7 \text{ M}_\odot$ of iron (e.g., Mazzali et al. 2007). We integrate over the SN Ia rate evolution derived from the convolving the power-law DTD described in the previous section with the Y08 SFH, multiplied by the above iron yield, to derive the amount of iron produced by SNe Ia. The uncertainty in the amount of iron contributed by SNe Ia

is calculated by integrating the upper and lower bounds of the shaded area in Fig. 13, multiplied by the above iron yield. This takes into account both the spread in the SN Ia rate measurements, and the plausible range of SFH shapes. We calculate the amount of iron produced by CC SNe by integrating over the Y08 SFH fit. Using the Salpeter (1955) IMF (as assumed by Y08), we calculate either the number of stars with masses $8 < M < 50 \text{ M}_\odot$ or the mass in such stars. If we assume that 1 per cent of the CC SN progenitor mass is converted into iron (as in Maoz et al. 2010b), then the present-day ratio of iron mass produced by SNe Ia to that produced by CC SNe is 1:2. If, on the other hand, we assume that each CC SN produces, on average, 0.066 M_\odot of iron (as in Blanc & Greggio 2008, based on CC SN samples from Zampieri et al. 2003 and Hamuy 2003), then the ratio increases to 1:1. As the major source of uncertainty in the amount of iron contributed by CC SNe is the normalization of the SFH, we integrate over the B10n and HB06c SFHs to derive upper and lower bounds on the uncertainty region. Finally, we sum the lower (upper) uncertainty bounds of the separate SN Ia and CC SN contributions to arrive at lower (upper) limits on the total cosmic density of iron.

Both scenarios are presented in Fig. 14. The mean cosmic iron abundance in solar units, marked on the left ordinate axis, is calculated assuming $\Omega_b = 0.0445$ for the baryon density in units of the critical closure density (Komatsu et al. 2010), and $Z_{\text{Fe},\odot} = 1.3 \pm 0.1 \times 10^{-3}$ for the solar iron abundance (Grevesse & Sauval 1998). We see that the present-day mean cosmic iron abundance lies in the range $0.06\text{--}0.37 Z_{\text{Fe},\odot}$. Between $z = 0$ and 2, for a given choice of SFH, the abundance behaves roughly linearly, e.g., as:

$$\begin{aligned} Z_{\text{Fe,L}} &\approx 0.29 - 0.08(1+z) \\ Z_{\text{Fe,R}} &\approx 0.16 - 0.05(1+z), \end{aligned} \quad (10)$$

for the best-fitting solid black curves in the left and right panels of Fig. 14, respectively. The choice of SFH propagates to a dominant systematic uncertainty in the CC SN contribution to the iron abundance.

Future probes of the metallicity of the intergalactic medium (IGM), in which most baryons in the Universe re-

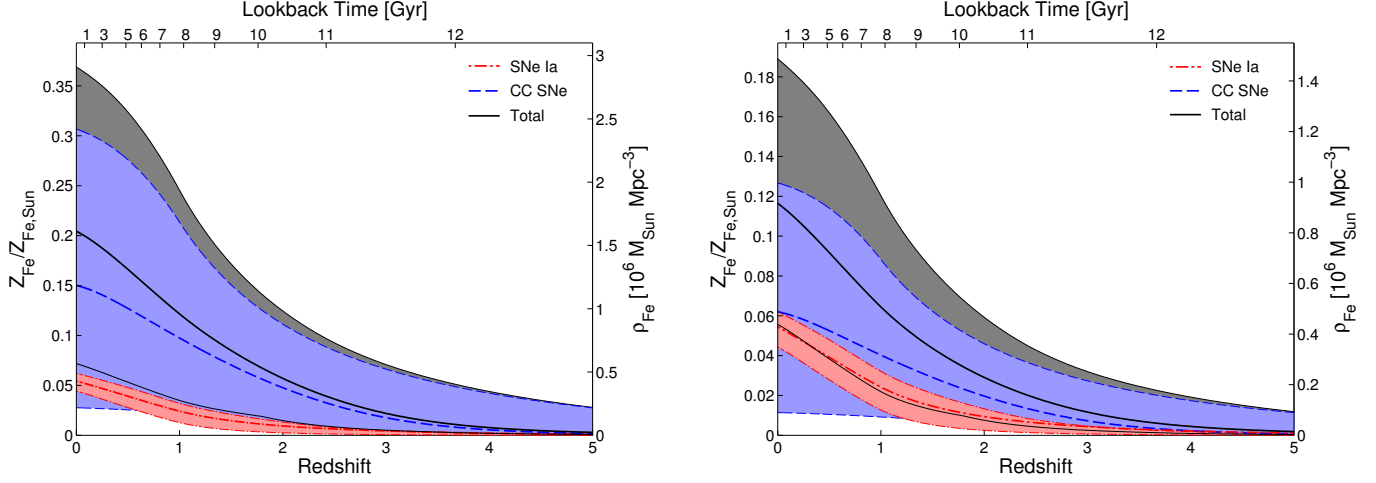


Figure 14. Cosmic iron density as a function of redshift. In both panels the SN Ia contribution is denoted by the dot-dashed line, the CC SN contribution by the dashed line, and the total amount of iron by the solid line. The dark region around the SN Ia contribution is the systematic and 68 per cent statistical uncertainty introduced by the SFH fits and the SN Ia rate measurements, respectively. The shaded region around the CC SN contribution is the result of the systematic uncertainty in the SFH fits alone. The dark region around the total iron density curve is the uncertainty introduced by both SN components. Thin lines delineate the uncertainty regions of each component. Left: assuming 1 per cent of the CC SN progenitor mass is converted into iron. Right: assuming each CC SN, on average, produces $0.066 M_{\odot}$ of iron.

side, and the evolution of this metallicity with redshift, can be compared with these predictions to constrain both the integrated iron production of CC SNe and the efficiency with which metals produced by SNe are ejected into the IGM.

10 CONCLUSIONS

By surveying four deep epochs of the 0.25 deg^2 SDF, we have assembled a sample of 150 SNe, of which 26 are SNe Ia at $1.0 < z < 1.5$, and 10 are SNe Ia at $1.5 < z < 2.0$. This is the largest sample of SNe Ia at such high redshifts to date. The number of SNe Ia in our $1.0 < z < 1.5$ bin is comparable to that of D08 in the same range, but our $1.5 < z < 2.0$ sample is 2.5 times as large. While we may have discovered some non-Ia transients in the redshift range $1.5 < z < 2.0$, we have argued that further contamination of our high- z SN Ia sample is unlikely. Through various tests, we have shown that the high- z SNe in our sample are securely associated with galaxies at these redshifts, and since our survey is mostly insensitive to CC SNe, they must be SNe Ia. The SN Ia rates derived from our sample are consistent with those of D08, but are 2-3 times more precise, with uncertainties of 30–50 per cent. Our measurements indicate that, following the rise at $0 < z < 1$, the SN Ia rate appears to level off after $z \approx 1$, but there is no evidence for a decline in the SN Ia rate evolution, of the form advocated by D08.

Based on these rates and on a growing number of accurate measurements at $z < 1$, and combined with different SFHs, we find that a power-law DTD of the form $\Psi(t) = \Psi_1(t/1 \text{ Gyr})^\beta$ fits the data well, with $\beta = -0.97^{+0.26(0.40)}_{-0.28(0.43)}$ (68 and 95 per cent statistical confidence, respectively) $^{+0.17}_{-0.18}$ (systematic). This form is consistent with the DTDs found by most of the recent SN Ia surveys, in a variety of environments, at different redshifts, and using different method-

ologies (Totani et al. 2008; Maoz et al. 2010a,b; Maoz & Badenes 2010). A $t^{-1/2}$ power law at all delay times, as proposed by Pritchett et al. (2008), is marginally consistent with the data. DTDs consisting of broken power laws are also acceptable, as long as t_c , the time at which the DTD transitions from a $t^{-1/2}$ power law to a t^{-1} power law, is less than ~ 5 Gyr (68 per cent confidence). The Gaussian DTD proposed by D04, D08, and Strolger et al. (2004, 2010) is ruled out by all but one of the SFHs tested here. Overall, these results are suggestive of the DD progenitor scenario, for which a power law with $\beta \approx -1$ is a generic prediction. The DD channel may not be the only one that produces SNe Ia, but it appears that a large fraction of SNe Ia are formed in this way, or in some other way that mimics the DTD predictions of the DD channel.

Using the best-fitting power-law DTD, we predict that the mean iron abundance of the universe has risen roughly linearly with $(1+z)$ over the past 10 Gyr, and is now in the range $0.06\text{--}0.37 Z_{\text{Fe},\odot}$. This prediction is consistent with those of Fukugita & Peebles (2004) and Blanc & Greggio (2008), but is now based on the most recent and accurate SN Ia rate measurements, the full range of plausible cosmic SFHs, and the current DTD estimations.

The time-integrated number of SNe Ia per unit mass derived from the best-fitting power-law DTD, assuming a ‘diet-Salpeter’ IMF (Bell et al. 2003), is in the range $N_{\text{SN}}/M_* = (0.74\text{--}5.4) \times 10^{-3} M_{\odot}^{-1}$. This is consistent with the values found in local galaxies by Maoz et al. (2010a) and in galaxy clusters by Maoz et al. (2010b).

The CC SN rate at $\langle z \rangle = 0.66$ is $3.3^{+4.0}_{-2.7} \times 10^{-4} \text{ yr}^{-1} \text{ Mpc}^{-3}$. This value is consistent with the only other measurement in this redshift range (D04), and shows that, as expected, the CC SN rate tracks the cosmic SFH out to $z \approx 1$.

Our survey in the SDF has reached the point where the

systematic uncertainties in the SN rates are comparable to the statistical uncertainties. The 1.5 deg² Hyper-Suprime Cam (Furusawa et al. 2010), soon to be installed on the Subaru Telescope, could allow discovery of larger numbers of SNe per epoch and thus a further reduction in the statistical uncertainties. A new SN survey in a well-studied field, such as the SDF or the SXDF, but with cadences designed to probe the light curves of the SNe, could permit classification of the SNe at a higher level of accuracy, thus reducing the systematic uncertainties as well. This will also apply to future massive surveys such as the Large Synoptic Survey Telescope (Stubbs et al. 2004) or the Synoptic All-Sky Infrared Survey (Bloom et al. 2009), for which traditional spectroscopic followup will be impossible, but to which the approach we have followed here is optimally suited.

Two *HST* Treasury programs — CLASH (GO12065-12069, GO12100-12104) and CANDELS (GO12060-12061) — have recently begun deep IR observations utilizing the *F125W* and *F160W* filters on the Wide Field Camera 3. These filters, equivalent to *J* and *H*, will probe the optical part of the SN spectrum out to $z \approx 1.5$, and the near-UV part of the spectrum out to $z \approx 2.5$. By observing the optical part of the spectrum in the observer-frame IR, one can reduce the uncertainties due to high-redshift dust, thus lowering the systematic uncertainty of the SN rates in the redshift range $1.0 < z < 1.5$. Ultimately, these programs will provide independent measurements of the SN Ia rate in the $1.0 < z < 2.0$ range probed by this work, as well as extend our knowledge of the SN Ia rate evolution out to $z \approx 2.5$. Based on the results presented here, as seen in Fig. 12, we predict that these programs will observe a similar number of SNe Ia at $z = 2.5$ as at $z = 1.5$.

ACKNOWLEDGMENTS

We thank Mamoru Doi for his contributions to this project, Robert Feldmann, Suzanne Hawley, Eric Hilton, Weidong Li, and Lucianne Walkowicz for helpful discussions and comments, and Masao Hayashi, Nobunari Kashikawa, Chun Ly, Matt Malkan, and Tomoki Morokuma for sharing their data. O.G. thanks Joshua Bloom for hosting him during a month-long visit to Berkeley. This work was based on data collected at the Subaru Telescope, which is operated by the National Astronomical Observatory of Japan. Additional data presented here were obtained at the W. M. Keck Observatory, which is operated as a scientific partnership among the California Institute of Technology, the University of California, and the National Aeronautics and Space Administration; the Observatory was made possible by the generous financial support of the W. M. Keck Foundation. The authors wish to recognize and acknowledge the very significant cultural role and reverence that the summit of Mauna Kea has always had within the indigenous Hawaiian community. We are most fortunate to have the opportunity to conduct observations from this mountain. This research has made use of NASA’s Astrophysics Data System (ADS) Bibliographic Services. This work was supported by a grant from the Israel Science Foundation (D.M). D.P. is supported by an Einstein Fellowship, and by the US Department of Energy Scientific Discovery through Advanced Computing (SciDAC) program under contract DE-FG02-06ER06-04. A.G. is sup-

ported by an FP7/Marie Curie IRG fellowship and a grant from the Israeli Science Foundation (ISF). A.V.F. is grateful for the financial support of NSF grant AST-0908886, the TABASGO Foundation, and Department of Energy grant DE-FG0-08ER41563.

REFERENCES

- Alard C., Lupton R. H., 1998, *ApJ*, 503, 325
- Arcavi I. et al., 2010, *ApJ*, 721, 777
- Astier P. et al., 2006, *A&A*, 447, 31
- Aubourg É., Tojeiro R., Jimenez R., Heavens A., Strauss M. A., Spergel D. N., 2008, *A&A*, 492, 631
- Badenes C., Mullally F., Thompson S. E., Lupton R. H., 2009, *ApJ*, 707, 971
- Barbary K. et al., 2009, *ApJ*, 690, 1358
- Barbary K. et al., 2010, preprint (arXiv:1010.5786)
- Barris B. J., Tonry J. L., 2006, *ApJ*, 637, 427
- Bazin G. et al., 2009, *A&A*, 499, 653
- Becker A. C. et al., 2004, *ApJ*, 611, 418
- Bell E. F., McIntosh D. H., Katz N., Weinberg M. D., 2003, *ApJS*, 149, 289
- Benson P. J. et al., 1994, *AJ*, 107, 1453
- Bertin E., Arnouts S., 1996, *A&AS*, 117, 393
- Blanc G. et al., 2004, *A&A*, 423, 881
- Blanc G., Greggio L., 2008, *NewA*, 13, 606
- Bloom J. S. et al., 2009, preprint (arXiv:0905.1965)
- Botticella M. T. et al., 2008, *A&A*, 479, 49
- Bouwens R. J., Illingworth G. D., Franx M., Ford H., 2008, *ApJ*, 686, 230
- Bouwens R. J. et al., 2010, preprint (arXiv:1006.4360)
- Brandt T. D., Tojeiro R., Aubourg É., Heavens A., Jimenez R., Strauss M. A., 2010, *AJ*, 140, 804
- Cappellaro E., Evans R., Turatto M., 1999, *A&A*, 351, 459
- Cappellaro E. et al., 2005, *A&A*, 430, 83
- Cole S. et al., 2001, *MNRAS*, 326, 255
- Cooke J. et al., 2010, preprint (arXiv:1010.2211)
- Cooper M. C., Newman J. A., Yan R., 2009, *ApJ*, 704, 687
- Daddi E. et al., 2005, *ApJ*, 631, L13
- Dahlen T., Strolger L., Riess A. G., 2008, *ApJ*, 681, 462
- Dahlen T. et al., 2004, *ApJ*, 613, 189
- de Vaucouleurs G., 1948, *Annales d’Astrophysique*, 11, 247
- Di Carlo E. et al., 2002, *ApJ*, 573, 144
- Dilday B. et al., *ApJ*, 682, 262
- Dilday B. et al., 2010a, *ApJ*, 713, 1026
- Dilday B. et al., 2010b, *ApJ*, 715, 1021
- Drout M. R. et al., 2010, preprint (arXiv:1011.4959)
- Faber S. M. et al., 2003, in *Society of Photo-Optical Instrumentation Engineers (SPIE) Conference Series*, Vol. 4841, *Society of Photo-Optical Instrumentation Engineers (SPIE) Conference Series*, M. Iye & A. F. M. Moorwood, ed., pp. 1657–1669
- Feldmann R. et al., 2006, *MNRAS*, 372, 565
- Filippenko A. V., 1997, *ARA&A*, 35, 309
- Foley R. J. et al., 2010, preprint (arXiv:1010.2749)
- Foley R. J., Smith N., Ganeshalingam M., Li W., Chornock R., Filippenko A. V., 2007, *ApJ*, 657, L105
- Freeman K. C., 1970, *ApJ*, 160, 811
- Fukugita M., Peebles P. J. E., 2004, *ApJ*, 616, 643
- Furusawa H. et al., 2010, in *Society of Photo-Optical Instrumentation Engineers (SPIE) Conference Series*, Vol.

- 7740, Society of Photo-Optical Instrumentation Engineers (SPIE) Conference Series
- Gal-Yam A., Maoz D., Sharon K., 2002, *MNRAS*, 332, 37
- Gal-Yam A., Maoz D., 2004, *MNRAS*, 347, 942
- Gal-Yam A., Poznanski D., Maoz D., Filippenko A. V., Foley R. J., 2004, *PASP*, 116, 597
- Gal-Yam A. et al., 2009, *Nature*, 462, 624
- Geier S., Nesslinger S., Heber U., Przybilla N., Napiwotzki R., Kudritzki R., 2007, *A&A*, 464, 299
- Giavalisco M. et al., 2004, *ApJ*, 600, L103
- González Hernández J. I., Ruiz-Lapuente P., Filippenko A. V., Foley R. J., Gal-Yam A., Simon J. D., 2009, *ApJ*, 691, 1
- Graham M. L. et al., 2008, *AJ*, 135, 1343
- Greggio L., 2005, *A&A*, 441, 1055
- Grevesse N., Sauval A. J., 1998, *Space Sci. Rev.*, 85, 161
- Hamuy M., 2003, *ApJ*, 582, 905
- Hamuy M., Phillips M. M., Maza J., Suntzeff N. B., Schommer R. A., Aviles R., 1995, *AJ*, 109, 1
- Hamuy M., Phillips M. M., Suntzeff N. B., Schommer R. A., Maza J., Aviles R., 1996, *AJ*, 112, 2398
- Han Z., Podsiadlowski P., 2004, *MNRAS*, 350, 1301
- Hardin D. et al., 2000, *A&A*, 362, 419
- Hayashi M. et al., 2009, *ApJ*, 691, 140
- Hillebrandt W., Niemeyer J. C., 2000, *ARA&A*, 38, 191
- Hoeflich P., Wheeler J. C., Thielemann F. K., 1998, *ApJ*, 495, 617
- Holwerda B. W., 2008, *MNRAS*, 386, 475
- Hopkins A. M., Beacom J. F., 2006, *ApJ*, 651, 142
- Horesh A., Poznanski D., Ofek E. O., Maoz D., 2008, *MNRAS*, 389, 1871
- Horiuchi S., Beacom J. F., 2010, *ApJ*, 723, 329
- Howell D. A., 2010, preprint (arXiv:1011.0441)
- Iben Jr. I., Tutukov A. V., 1984, *ApJS*, 54, 335
- Jha S. et al., 2006, *AJ*, 131, 527
- Kashikawa N. et al., 2004, *PASJ*, 56, 1011
- Kashikawa N. et al., 2003, *AJ*, 125, 53
- Kashikawa N. et al., 2006, *ApJ*, 637, 631
- Kerzendorf W. E. et al., 2009, *ApJ*, 701, 1665
- Kessler R. et al., 2009, *ApJS*, 185, 32
- Kiewe M. et al., 2010, preprint (arXiv:1010.2689)
- Kistler M. D., Yüksel H., Beacom J. F., Hopkins A. M., Wyithe J. S. B., 2009, *ApJ*, 705, L104
- Komatsu E. et al., 2010, preprint (arXiv:1001.4538)
- Kowalski A. F., Hawley S. L., Holtzman J. A., Wisniewski J. P., Hilton E. J., 2010, *ApJ*, 714, 98
- Kowalski A. F., Hawley S. L., Hilton E. J., Becker A. C., West A. A., Bochanski J. J., Sesar B., 2009, *AJ*, 138, 633
- Kuznetsova N. et al., 2008, *ApJ*, 673, 981
- Le Floch E. et al., 2005, *ApJ*, 632, 169
- Leaman J., Li W., Chornock R., Filippenko A. V., 2010, preprint (arXiv:1006.4611)
- Lentz E. J., Baron E., Branch D., Hauschildt P. H., Nugent P. E., 2000, *ApJ*, 530, 966
- Li W., Chornock R., Leaman J., Filippenko A. V., Poznanski D., Wang X., Ganeshalingam M., Mannucci F., 2010a, preprint (arXiv:1006.4613)
- Li W. et al., 2010b, preprint (arXiv:1006.4612)
- Madgwick D. S., Hewett P. C., Mortlock D. J., Wang L., 2003, *ApJ*, 599, L33
- Mannucci F., Della Valle M., Panagia N., 2006, *MNRAS*, 370, 773
- , 2007, *MNRAS*, 377, 1229
- Mannucci F., Della Valle M., Panagia N., Cappellaro E., Cresci G., Maiolino R., Petrosian A., Turatto M., 2005, *A&A*, 433, 807
- Mannucci F., Maoz D., Sharon K., Botticella M. T., Della Valle M., Gal-Yam A., Panagia N., 2008, *MNRAS*, 383, 1121
- Maoz D., Badenes C., 2010, *MNRAS*, 968
- Maoz D., Mannucci F., Li W., Filippenko A. V., Della Valle M., Panagia N., 2010a, preprint (arXiv:1002.3056)
- Maoz D., Sharon K., Gal-Yam A., 2010b, *ApJ*, 722, 1879
- Matteucci F., Spitoni E., Recchi S., Valiante R., 2009, *A&A*, 501, 531
- Mazzali P. A. et al., 2007, *ApJ*, 670, 592
- Mennekens N., Vanbeveren D., De Greve J. P., De Donder E., 2010, *A&A*, 515, A89+
- Miyazaki S. et al., 2002, *PASJ*, 54, 833
- Napiwotzki R. et al., 2004, in *Astronomical Society of the Pacific Conference Series*, Vol. 318, *Spectroscopically and Spatially Resolving the Components of the Close Binary Stars*, R. W. Hilditch, H. Hensberge, & K. Pavlovski, ed., pp. 402–410
- Neill J. D. et al., 2006, *AJ*, 132, 1126
- , 2007, in *American Institute of Physics Conference Series*, Vol. 924, *The Multicolored Landscape of Compact Objects and Their Explosive Origins*, T. di Salvo, G. L. Israel, L. Piersant, L. Burderi, G. Matt, A. Tornambe, & M. T. Menna, ed., pp. 421–424
- Nugent P., Kim A., Perlmutter S., 2002, *PASP*, 114, 803
- Oda T., Totani T., Yasuda N., Sumi T., Morokuma T., Doi M., Kosugi G., 2008, *PASJ*, 60, 169
- Oke J. B. et al., 1995, *PASP*, 107, 375
- Oke J. B., Gunn J. E., 1983, *ApJ*, 266, 713
- Ouchi M. et al., 2004, *ApJ*, 611, 660
- Pain R. et al., 2002, *ApJ*, 577, 120
- Peng C. Y., Ho L. C., Impey C. D., Rix H., 2002, *AJ*, 124, 266
- , 2010, *AJ*, 139, 2097
- Perets H. B. et al., 2010, *Nature*, 465, 322
- Pérez-González P. G. et al., 2005, *ApJ*, 630, 82
- Perlmutter S. et al., 1999, *ApJ*, 517, 565
- Petrosian V., 1976, *ApJ*, 209, L1
- Phillips M. M., Lira P., Suntzeff N. B., Schommer R. A., Hamuy M., Maza J., 1999, *AJ*, 118, 1766
- Poznanski D., Gal-Yam A., Maoz D., Filippenko A. V., Leonard D. C., Matheson T., 2002, *PASP*, 114, 833
- Poznanski D., Maoz D., Gal-Yam A., 2007a, *AJ*, 134, 1285
- Poznanski D. et al., 2007b, *MNRAS*, 382, 1169
- Pritchett C. J., Howell D. A., Sullivan M., 2008, *ApJ*, 683, L25
- Quimby R. M., Aldering G., Wheeler J. C., Höflich P., Akserlof C. W., Rykoff E. S., 2007, *ApJ*, 668, L99
- Quimby R. M. et al., 2009, preprint (arXiv:0910.0059)
- Raskin C., Scannapieco E., Rhoads J., Della Valle M., 2009, *ApJ*, 707, 74
- Reddy N. A., Steidel C. C., 2009, *ApJ*, 692, 778
- Richardson D., Branch D., Casebeer D., Millard J., Thomas R. C., Baron E., 2002, *AJ*, 123, 745
- Riess A. G. et al., 2004, *ApJ*, 600, L163
- Robertson B. E., Ellis R. S., Dunlop J. S., McLure R. J., Stark D. P., 2010, *Nature*, 468, 49
- Rodney S. A., Tonry J. L., 2010, *ApJ*, 723, 47

- Roelofs G., Bassa C., Voss R., Nelemans G., 2008, MNRAS, 391, 290
- Ruiter A. J., Belczynski K., Fryer C., 2009, ApJ, 699, 2026
- Rujopakarn W. et al., 2010, ApJ, 718, 1171
- Salpeter E. E., 1955, ApJ, 121, 161
- Sauer D. N. et al., 2008, MNRAS, 391, 1605
- Scannapieco E., Bildsten L., 2005, ApJ, 629, L85
- Sersic J. L., 1968, Atlas de galaxias australes, Sersic J. L., ed.
- Sharon K., Gal-Yam A., Maoz D., Filippenko A. V., Guhathakurta P., 2007, ApJ, 660, 1165
- Sharon K. et al., 2010, ApJ, 718, 876
- Shimasaku K. et al., 2006, PASJ, 58, 313
- Smartt S. J., 2009, ARA&A, 47, 63
- Smartt S. J., Eldridge J. J., Crockett R. M., Maund J. R., 2009, MNRAS, 395, 1409
- Smith N. et al., 2007, ApJ, 666, 1116
- Stern S. A., Colwell J. E., 1997, ApJ, 490, 879
- Strolger L., Dahlen T., Riess A. G., 2010, ApJ, 713, 32
- Strolger L. et al., 2004, ApJ, 613, 200
- Stubbs C. W., Sweeney D., Tyson J. A., LSST, 2004, in Bulletin of the American Astronomical Society, Vol. 36, Bulletin of the American Astronomical Society, pp. 1527–+
- Sullivan M. et al., 2006, AJ, 131, 960
- Tody D., 1986, in Society of Photo-Optical Instrumentation Engineers (SPIE) Conference Series, Vol. 627, Society of Photo-Optical Instrumentation Engineers (SPIE) Conference Series, D. L. Crawford, ed., pp. 733–+
- Tonry J. L. et al., 2003, ApJ, 594, 1
- Totani T., Morokuma T., Oda T., Doi M., Yasuda N., 2008, PASJ, 60, 1327
- Verma A., Lehnert M. D., Förster Schreiber N. M., Bremer M. N., Douglas L., 2007, MNRAS, 377, 1024
- Voss R., Nelemans G., 2008, Nature, 451, 802
- Walkowicz L. M. et al., 2010, preprint (arXiv:1008.0853)
- Wang L., Strovink M., Conley A., Goldhaber G., Kowalski M., Perlmutter S., Siegrist J., 2006, ApJ, 641, 50
- Webbink R. F., 1984, ApJ, 277, 355
- West A. A., Hawley S. L., Bochanski J. J., Covey K. R., Reid I. N., Dhital S., Hilton E. J., Masuda M., 2008, AJ, 135, 785
- Whelan J., Iben Jr. I., 1973, ApJ, 186, 1007
- Yagi M., Kashikawa N., Sekiguchi M., Doi M., Yasuda N., Shimasaku K., Okamura S., 2002, AJ, 123, 66
- Yan H., Windhorst R., Hathi N., Cohen S., Ryan R., O’Connell R., McCarthy P., 2009, RAA, 10, 867
- Yasuda N., Fukugita M., 2010, AJ, 139, 39
- York D. G. et al., 2000, AJ, 120, 1579
- Yüksel H., Kistler M. D., Beacom J. F., Hopkins A. M., 2008, ApJ, 683, L5
- Yungelson L. R., Livio M., 2000, ApJ, 528, 108
- Zampieri L., Ramina M., Pastorello A., 2003, preprint (ArXiv:astro-ph/0310057)

Table 7. SNe discovered in the SDF. The full table, including all epochs, is available in the electronic version of the paper.

ID (1)	α (2)	δ (3)	Offset (4)	R (5)	i' (6)	z' (7)	S/N (8)	Photo- z (9)	χ^2 (10)	Spec- z (11)	P_{Ia} (12)	Post- z (13)	χ^2 (14)	Type (15)	Adopted- z (16)
SNSDF0503.01	23:52.41	12:45.21	0.14(04)	24.06(02)	23.65(02)	23.57(04)	47	0.90	2.96	0.886	1.00	0.89	1.31	Ia	0.89
SNSDF0503.02	24:45.54	18:13.98	0.20(06)	23.58(02)	23.74(02)	23.71(03)	38	0.32	0.99	...	0.79	0.29	0.07	Ia	0.29
SNSDF0503.03	24:22.02	16:07.00	0.39(02)	24.17(03)	23.93(02)	23.74(03)	45	0.70	2.65	0.593	0.98	0.59	0.07	Ia	0.59
SNSDF0503.04	25:14.55	29:16.48	0.31(03)	24.76(05)	24.22(03)	24.03(04)	44	0.90	0.89	0.918	0.99	0.92	0.75	Ia	0.92
SNSDF0503.05	25:33.34	36:39.61	0.28(03)	24.59(04)	24.26(03)	24.03(04)	32	0.75	10.37	0.707	0.88	0.70	0.56	Ia	0.71
...															
...															

(1) – SN identification.

(2)–(3) – Right ascensions (J2000; starting at 13^h) and declinations (J2000; starting at +27°).

(4) – SN offset from host galaxy, in arcseconds. Uncertainties appear in parenthesis, and have been multiplied by 100.

(5)–(7) – SN photometry in the R , i' , and z' bands, in magnitudes. Uncertainties appear in parenthesis, and have been multiplied by 100.(8) – Signal-to-noise ratio of the SN, as measured in the z' -band image.(9)–(10) – Photometric redshift of SN host galaxy, with reduced χ^2 , as derived with ZEBRA.

(11) – Spectroscopic redshift of SN host galaxy, where available.

(12)–(14) – Probability of a SN being a Type Ia, or CC SN, as derived with the SNABC, together with its posterior redshift and reduced χ^2 .

(15)–(16) – Final adopted SN type and redshift.

Table 8. SN host galaxies. The full table, including all epochs, is available in the electronic version of the paper.

ID (1)	α (2)	δ (3)	FUV (4)	NUV (5)	B (6)	V (7)	R (8)	i' (9)	z' (10)	$NB816$ (11)	$NB921$ (12)	J (13)	K (14)
hSDF0503.01	23:52.42	12:45.31	−1	1	25.35(05)	25.14(08)	25.14(08)	24.66(07)	24.64(10)	24.65(11)	24.37(10)
hSDF0503.02	24:45.56	18:14.01	−1	0	27.34(19)	26.38(19)	26.22(16)	26.07(18)	25.78(22)	> 26.63	> 26.54
hSDF0503.03	24:22.04	16:07.26	−1	0	24.62(03)	24.24(04)	23.48(02)	23.21(03)	23.06(03)	23.15(03)	23.22(04)	22.69(11)	22.88(10)
hSDF0503.04	25:14.53	29:16.46	−1	0	24.35(02)	23.83(03)	23.25(02)	22.43(03)	21.98(02)	22.19(01)	22.06(01)	...	20.50(03)
hSDF0503.05	25:33.32	36:39.76	−1	1	23.79(02)	23.63(03)	23.08(02)	22.79(03)	22.73(02)	22.73(02)	22.91(03)	23.30(18)	22.95(11)
...													
...													

Note - magnitude limits are 3σ .

(1) – SN identification.

(2)–(3) – Right ascensions (J2000; starting at 13^h) and declinations (J2000; starting at +27°).(4)–(5) – *GALEX* FUV and NUV photometry. −1 means no UV signal observed in this band; 1 means a clear UV signal associated with the target galaxy; and 0 means the UV signal could not be unequivocally matched to the target galaxy.

(6)–(12) – Subaru optical photometry, in magnitudes. Uncertainties appear in parenthesis, and have been multiplied by 100.

(13)–(14) – UKIRT J and K photometry, in magnitudes. Uncertainties appear in parenthesis, and have been multiplied by 100.